

Chapter 4

Electronic properties of nanostructures: Tunneling & Josephson effects

The description of tunneling of particles through barriers is one of the milestones of quantum mechanics, and treated in every basic course of quantum mechanics. The physics of tunneling applies to many different fields, ranging from particle physics (e.g. nuclear fusion or radioactive α -decay) to astrochemistry, biology and solid state systems. In the latter, the tunnel junction, i.e. a device where electrons can tunnel through a barrier (insulator or vacuum) plays an important role for applications, such as the tunnel diode or the scanning tunneling microscope. First attempts to experimentally confirm tunneling of electrons through a thin insulating barrier separating two metallic electrodes have been made by Ivar Giaever and coworkers in the 1950s. A major difficulty in those experiments was to prove that the measured current-voltage characteristics (IVC) are indeed due to tunneling rather than metallic conduction through shorts in the barrier – both give rise to a linear IVC. This lead Giaever to use superconducting electrodes, for which non-linear IVCs in tunneling devices could be expected. This approach was a major success, as it provided not only an experimental proof of tunneling of electrons in solid state devices, but it also provided a clear experimental proof of the existence of an energy gap for the excitation of unpaired electrons (quasiparticles) in superconductors, as predicted by Bardeen, Cooper and Schrieffer within the first microscopic theory of superconductivity (BCS-Theory).¹ When Giaever stepped out of physics in the early 1960s, a young student at Cambridge University stepped in - Brian Josephson. He predicted in his theoretical work, that not only tunneling of single electrons, but also tunneling of Cooper pairs (the charge carriers in superconductors) can be significant. This work provided the foundation of superconducting electronics, based on the Josephson junction (two superconducting electrodes separated by a weak link, e.g. an insulating tunneling barrier), with a large variety of applications, e.g. in high-speed computing, quantum computing (Google, IBM), quantum sensing of magnetic fields and radioastronomy, to name just a few.

In this chapter, we will discuss the basics of tunneling of electrons through insulating barriers between normal metals and superconductors (Sec. 4.1) and then treat in

¹For his achievements, Ivar Giaever was awarded the Nobel prize in physics 1973.

Sec. 4.2 tunneling of Cooper pairs (Josephson effects) and a prominent device based on this – the superconducting quantum interference device (SQUID) – which is used in many fields of applications, ranging from biomagnetism and geophysical survey, to metrology, scanning probe microscopy and frequency-tunable superconducting quantum bits.

4.1 Tunneling effects (metals, superconductors)

In this section, we consider electric transport based on the tunneling of electrons through barriers between metallic or superconducting electrodes. To start with, we consider first the tunneling between metallic electrodes.

4.1.1 Tunneling through barriers & metallic tunnel junctions

The **tunneling effect** is a quantum mechanical process, and is based on the fact that the **probability density** $\Psi^*\Psi$ for the **wave function** Ψ remains **continuous** even at discontinuous potential steps.

This leads, e.g., at a **metall/vacuum interface** ($x = 0$) to a wave function for an electron (with Fermi energy E_F), which does not disappear outside the metal; instead, its amplitude decays exponentially with increasing distance x from the interface – i.e. in the classically forbidden regime – with $|\Psi| \propto \exp\{-\kappa x\}$.

Here, the **inverse decay length** is given as $\kappa \cong (2m/\hbar^2)^{1/2}\phi^{1/2}$, with the electron mass m and the work function² ϕ of the metal.^{3, 4}

In the following we consider **tunneling of electrons through insulating (I) barriers**. Here, the **electrode materials** can be **metallic** (N: normal conductor), or e.g. **ferromagnetic** (F), or **superconducting** (S).

For tunneling of **quasiparticles**⁵ between superconducting electrodes, the modified density of states (as compared to the normal metallic state) – and in particular the emergence of an **energy gap in the excitation spectrum** of the quasiparticles – plays an important role.

In the case of **F-electrodes**, the **disappearance of the degeneracy of spin states in the density of states** plays a decisive role. This can lead to different density of states for spin-up and spin-down electrons at the Fermi level, which corresponds to a finite spin polarization.

²Difference between vacuum level and E_F

³E. L. Wolf, *Principles of electron tunneling spectroscopy*, Oxford Univ. Press (New York), 1985.

⁴Obviously, tunneling processes are not restricted to the transport of electrons (famous example: emission of α particles at the decay of heavy nuclei; already in 1928 identified as tunneling process).

⁵Unpaired electrons in a superconductor

basic distinctions in the theoretical treatment of electron tunneling:

- **elastic vs. inelastic** tunneling:

elastic tunneling → energy of the electron does not change during the tunneling process

inelastic tunneling → electron gains or loses energy during tunneling due to excitation or absorption of elementary excitations in a solid (phonons, magnons, plasmons, ...)

- **1-dimensional vs. 3-dimensional** tunneling:

for simplification one often assumes a 1-dim. potential barrier

→ often sufficiently good approximation for the treatment of planar metal/insulator/metal tunnel junctions

→ other tunneling structures (e.g. tip on a planar surface)
however require the treatment of the the 3-dim. problem

- **rectangular** potential barrier vs. **arbitrarily shaped** potential barrier:

rectangular barrier can be treated much more easily;
however, is often a bad approximation for real tunneling structures

Fields of applications:

- Tunneling spectroscopy as a characterization method (in particular, scanning tunneling spectroscopy with high spatial resolution)
- Devices (e.g. Josephson junctions, magnetic tunnel junctions, ...)

Elastic tunneling through 1-dim. rectangular barrier

We consider the situation shown in Fig. 4.1, where an electron with energy E and mass m hits a barrier (thin insulating layer) of height U_0 and thickness d .

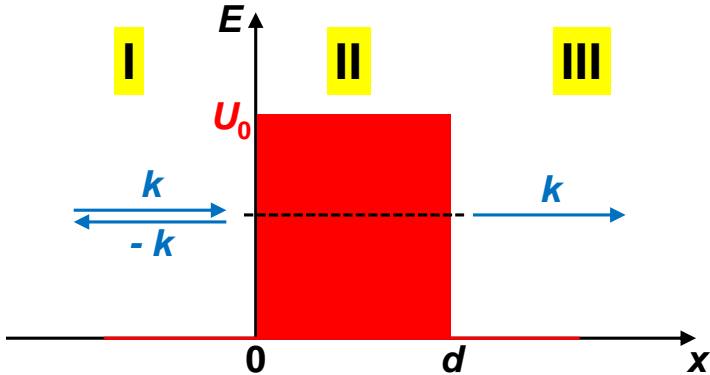


Fig. 4.1: One-dimensional, rectangular potential barrier with height U_0 and thickness d .

For the three sections I, II and III one obtains the following time-independent Schrödinger equations and the corresponding Ansatz for the electron wave functions $\Psi(x)$:

section I:

$$-\frac{\hbar^2}{2m} \frac{\partial^2 \Psi_I}{\partial x^2} = E \Psi_I \quad (4.1)$$

with

$$\Psi_I = e^{ikx} + A e^{-ikx} \quad \text{with} \quad k^2 = 2mE/\hbar^2 \quad (4.2)$$

section II:

$$-\frac{\hbar^2}{2m} \frac{\partial^2 \Psi_{II}}{\partial x^2} + U_0 \Psi_{II} = E \Psi_{II} \quad (4.3)$$

with

$$\Psi_{II} = B e^{-\kappa x} + C e^{\kappa x} \quad \text{with} \quad \kappa^2 = 2m(U_0 - E)/\hbar^2 \quad (4.4)$$

section III:

$$-\frac{\hbar^2}{2m} \frac{\partial^2 \Psi_{III}}{\partial x^2} = E \Psi_{III} \quad (4.5)$$

with

$$\Psi_{III} = D e^{ikx} \quad (4.6)$$

\Rightarrow an incident wave e^{ikx} from left

- is reflected with amplitude A at $x = 0$,
- decays exponentially as $e^{-\kappa x}$ inside the barrier ($0 < x < d$)
- and propagates with $D e^{ikx}$ at the right side of the barrier ($x > d$).

The ratio of transmitted (J_t) over incident (J_i) electron current yields the **transmissions coefficient**, or **tunneling probability**

$$T_m \equiv \frac{J_t}{J_i} = |D|^2 \quad (4.7)$$

(= probability for a particle to go through the barrier).

The **total wave function** follows then from the **continuous matching of the solutions at the potential steps**,⁶

i.e. by considering the corresponding boundary conditions
(continuity of Ψ and $\partial\Psi/\partial x$ at the insulator/electrode interfaces at position $x = 0, d$)

With this wave function, one can then determine T_m .

Within the frequently used **approximation** $d \gg \kappa^{-1}$ follows⁷

$$T_m = \left(\frac{4k\kappa}{k^2 + \kappa^2} \right)^2 e^{-2\kappa d} \quad (4.8)$$

→ the tunneling probability and hence the tunneling current
decays **exponentially** with increasing thickness d of the potential barrier.

The **inverse decay length** $\kappa = [2m(U_0 - E)]^{1/2}/\hbar$
is determined by the **effective height** ($U_0 - E$) of the potential barrier.

For typical heights of the potential barrier in the eV range \Rightarrow decay length $1/\kappa \approx 1 \text{ \AA}$

\Rightarrow exponential factor in (4.8) becomes very small
already for barrier thicknesses of a few \AA .

\Rightarrow **strong dependence of the tunneling current on barrier thickness d**
already for changes of d in the \AA range.

⁶This approach depicted here is also called the *wave matching* method, as one solves the Schrödinger equation in different sections and then matches the solutions continuously.

⁷E. L. Wolf, *Principles of electron tunneling spectroscopy*, Oxford Univ. Press (New York), 1985.

Tunneling current I as a function of applied voltage V

Measured quantities in tunneling experiments:

- tunneling current $I(V)$
 - or its derivative, the **differential tunneling conductance** $G(V) \equiv \partial I / \partial V$
 - or the inverse quantity $\partial V / \partial I$ (tunneling resistance)
- as a function of the voltage drop V across the barrier.

If $V = 0 \rightarrow$ Fermi energy E_F is the same for both electrodes.

If $V \neq 0$ (applied voltage) \rightarrow **energy difference** eV between the Fermi energies of the two electrodes.

Convention:

Positive voltage V lowers the right electrode (2) with respect to the left (1) by energy eV .

The **tunneling current** I_{12} from electrode (1) to electrode (2) is determined by:⁸

$$\text{number of tunneling electrons} \propto \begin{aligned} &\text{number of occupied states in (1)} \\ &\times \text{number of unoccupied states in (2)} \\ &\times \text{tunneling probability } T_m \end{aligned}$$

and vice versa for the current I_{21} from (2) to (1).

- \Rightarrow measuring the tunneling characteristics $I(V)$ can yield important information on the electronic structure of the electrode materials and the barrier;
- \rightarrow in particular, this allows one to draw conclusions on the **densities of states** $D_i(E)$ (resolution is limited by the thermal energy $k_B T$)

In the following we consider only **elastic tunneling processes** (energy of the charge carriers remains unchanged in the tunneling process)

\Rightarrow **tunneling current** I_{12} from left electrode (1) to right electrode (2):

$$I_{12} \propto \int_{-\infty}^{+\infty} T_m(\epsilon) \times D_1(\epsilon - eV) f(\epsilon - eV) \times D_2(\epsilon) \{1 - f(\epsilon)\} d\epsilon \quad (4.9)$$

and **tunneling current** I_{21} from right electrode (2) to left electrode (1):

$$I_{21} \propto \int_{-\infty}^{+\infty} T_m(\epsilon) \times D_2(\epsilon) f(\epsilon) \times D_1(\epsilon - eV) \{1 - f(\epsilon - eV)\} d\epsilon, \quad (4.10)$$

with **energy** $\epsilon \equiv E - E_F$ (i.e., referred to the Fermi level E_F of the respective electrode)
 \rightarrow integration goes from $-\infty$ to $+\infty$; $f(\epsilon)$ is the **Fermi distribution**

$$f(\epsilon) \equiv \frac{1}{\exp\{\epsilon/k_B T\} + 1} \quad . \quad (4.11)$$

The difference (4.9)–(4.10) yields then the **net tunneling current**:

$$I \equiv I_{12} - I_{21} \propto \int_{-\infty}^{+\infty} T_m(\epsilon) \times D_1(\epsilon - eV) D_2(\epsilon) \times [f(\epsilon - eV) - f(\epsilon)] d\epsilon. \quad (4.12)$$

⁸Follows from Fermi's golden rule

So far, our considerations are generally valid for arbitrary density of states. In the following, we consider the

normal conductor/insulator/normal conductor (NIN) junction:

Both electrodes ' N_i ' ($i=1,2$) shall be normal conducting (metallic).

We make the following **assumptions**:

- the energy dependence of the density of states D_{N_i} near the Fermi level shall be negligible, i.e., we set $D_{N_i}(E) = D_{N_i}(E_F) = \text{const}$ (free electron gas in 3-D: $D(E) \propto \sqrt{E}$)
- the tunneling probability T_m shall not depend on the energy E , i.e., we set $T_m(E) = T_m(E_F) = \text{const}$ (high barrier, independent of V)

With this, from Eq. (4.12) follows

$$I \propto \underbrace{D_{N_1}(E_F)D_{N_2}(E_F)T_m(E_F)}_{=\text{const.}} \int_{-\infty}^{+\infty} [f(\epsilon - eV) - f(\epsilon)]d\epsilon \quad . \quad (4.13)$$

$\underbrace{\qquad\qquad\qquad}_{\propto eV}$

⇒ **linear tunneling characteristics** $I \propto V$, i.e., voltage-independent tunneling conductance $(\partial I / \partial V)_{NN} \equiv G_{NN} \propto D_{N_1}(E_F)D_{N_2}(E_F) \approx \text{const}$

(for the case that the temperature $T = 0$
or – if V does not become too large – also for the case of finite temperature $T \neq 0$)

Illustration by the schematic $E(D)$ diagram in Fig. 4.2:

→ number of occupied states in electrode (1)
which are facing unoccupied states in electrode (2)
increases linearly with V .

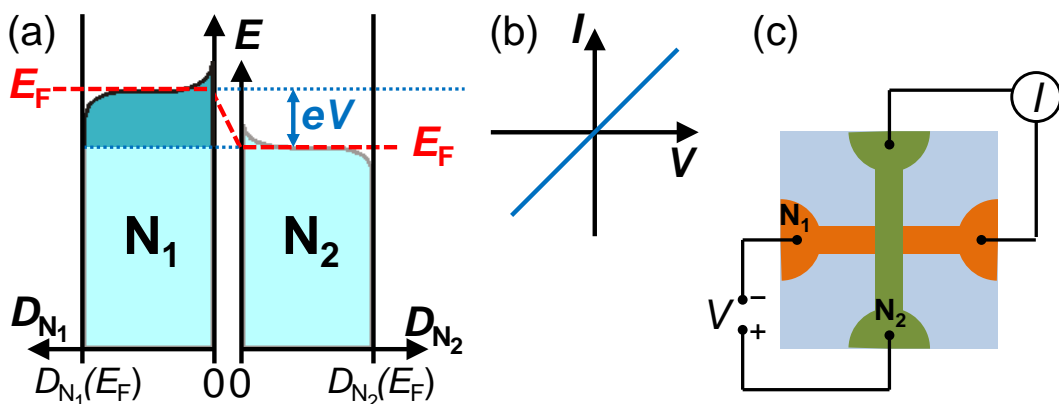


Fig. 4.2: N/I/N junction: (a) Density of states diagrams $E(D_{N_i})$ for two metallic electrodes N_1, N_2 . The colored areas represent the density of occupied states $D(E)f(E,T)$. (b) IV-characteristics. (c) Sample layout for a tunneling experiment (top view): two thin film bridges are separated by a thin insulating tunneling barrier.

Appendix: Tunneling with finite barrier height:

If one considers a finite barrier height, the rectangular potential formed by the insulator of thickness d is tilted by an applied voltage V , forming a trapezoid shape.

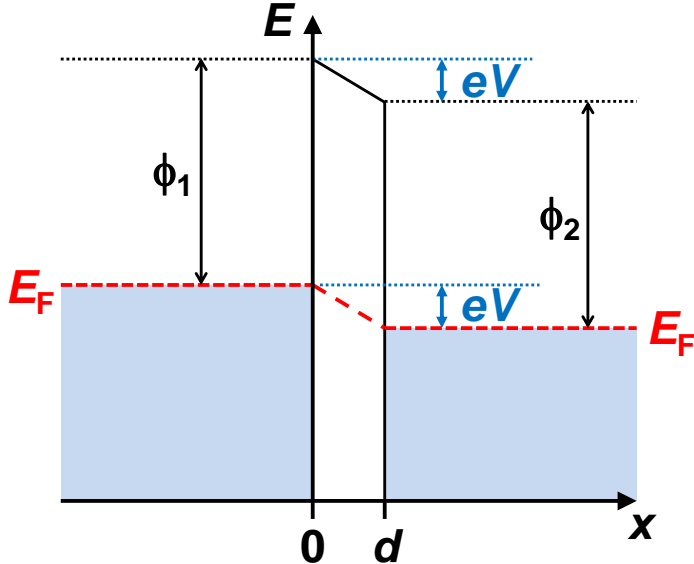


Fig. Z.1: N/I/N junction with finite barrier height.

With the assumption of **identical electrode materials**

(same work function $\phi_1 = \phi_2 \equiv \phi_0$ measured from the Fermi level)
follows the **potential of the barrier**

$$\phi(x, V) = \phi_0 - \frac{x}{d} \cdot eV \quad . \quad (4.14)$$

The wave function of an electrons decays inside the barrier ($0 < x < d$) as

$$|\psi| \propto \exp\left\{-\sqrt{\frac{2m}{\hbar^2}}[\phi(x, V) - E]\right\}$$

$\Rightarrow V$ -dependent transmission probability $T(\epsilon, V)$.

Model by Simmons, Brinkmann: ^a

For the case

- **small voltage:** $eV \ll \phi_0$ and $eV \ll E_F$
 - **thick barrier** $\frac{2}{\hbar}d\sqrt{2m(\phi_0 + eV)} \gg 1$
- \Rightarrow quadratic dependence of the normalized differential tunneling conductance

$$\frac{G_{NN}(V)}{G_{NN}(0)} = 1 + \left(\frac{e^2 m}{4\hbar^2} \frac{d^2}{\phi_0}\right) V^2. \quad (4.15)$$

Here, the absolute tunneling conductance at $V = 0$ is

$$G_{NN}(0) = \frac{\sqrt{2m\phi_0}}{d} \left(\frac{e}{\hbar}\right)^2 \exp\left\{-\frac{2\sqrt{2m}}{\hbar} d\phi_0^{1/2}\right\}. \quad (4.16)$$

\Rightarrow **Measurement of the differential tunneling conductance**

enables with the help of Eqs. (4.15) and (4.16)

to **determine the barrier height ϕ_0 and the barrier thickness d .**

^aE. L. Wolf, *Principles of electron tunneling spectroscopy*, Oxford Univ. Press (New York), 1985.

4.1.2 Superconductors: Quasiparticle tunneling

We consider now elastic tunneling of unpaired electrons ("quasiparticles") in normal conductor/insulator/superconductor (NIS) and superconductor/insulator/superconductor (SIS) tunnel junctions.

This is based on the general considerations, as discussed in Sec. 4.1.1 for the description of tunneling through barriers; i.e. in particular, that the insulating tunnel barrier has to be sufficiently thin (typically $\sim 1\text{ nm}$), so that the overlap of the wave functions between the electrodes leads to a finite probability for tunneling through the barrier.

For the density of states $D_S(\epsilon)$ of the quasiparticles in a superconductor follows from the Bardeen-Cooper-Schrieffer (BCS) theory

$$D_S(\epsilon) = D_N(0) \frac{|\epsilon|}{\sqrt{\epsilon^2 - \Delta^2}} \quad \text{if} \quad |\epsilon| \geq \Delta \\ D_S(\epsilon) = 0 \quad \text{if} \quad |\epsilon| < \Delta . \quad (4.17)$$

Here, Δ is the energy gap for quasiparticle excitations in the superconductor, and D_N is the density of states of the material in the normal conducting state. The energy is again referred to the Fermi level, i.e. $\epsilon = E - E_F$. The shape of $D_S(\epsilon)$ is shown in Fig. 4.3. The density of states D_S disappears within the energy gap $|\epsilon| < \Delta$ around the Fermi energy. At energies $\epsilon = \pm\Delta$, the density of states diverges and for further increasing values of $|\epsilon|$, D_S approaches rapidly the density of states $D_N(0)$ for the normal conducting state. Within the BCS approximation one has the relation $2\Delta(T \ll T_c) \approx 3.5 k_B T_c$ (T_c : transition temperature).

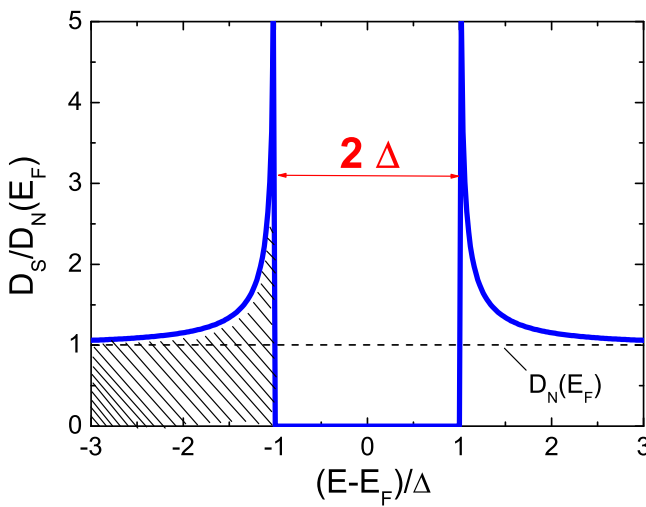


Fig. 4.3: quasiparticle density of states D_S vs energy $\epsilon = E - E_F$ for a superconductor with energy gap Δ . The energy is normalized to Δ and the density of states to the value D_N in the normal conducting state at E_F .

Due to the drastically modified quasiparticle density of states in superconductors, we can expect a significant change of the tunneling characteristics, if one or both metallic electrodes undergo a transition into the superconducting state.

NIS junction:

In the following, we consider the case that one of the two electrodes is superconducting, i.e., we have a NIS junction. With the help of the corresponding density of states diagram in Fig. 4.4(a), one can easily understand the shape of the IV characteristics, which is significantly modified as compared to that of a NIN junction. Figure 4.4(a) shows the situation with applied voltage V , which lowers the states of the S electrode by $eV < \Delta$.

Upon applying a voltage $V < V_g = \Delta/e$ (V_g is denoted as the ‘gap voltage’) [see Fig. 4.4(a)], initially there flows no (for $T = 0$), or only a very small (for finite T) tunneling current. This is because due to the energy gap in the S electrode there are no unoccupied quasiparticle states available. Only when $eV = \Delta$ is reached, the tunneling current increases strongly, as then occupied states at the Fermi level in the normal conductor are facing a high density of unoccupied quasiparticle states in the superconductor. For $eV \gg \Delta$, the tunneling characteristics again approaches (within the simplest approximation) the linear characteristics of a NIN junction (see Fig. 4.4(b)).

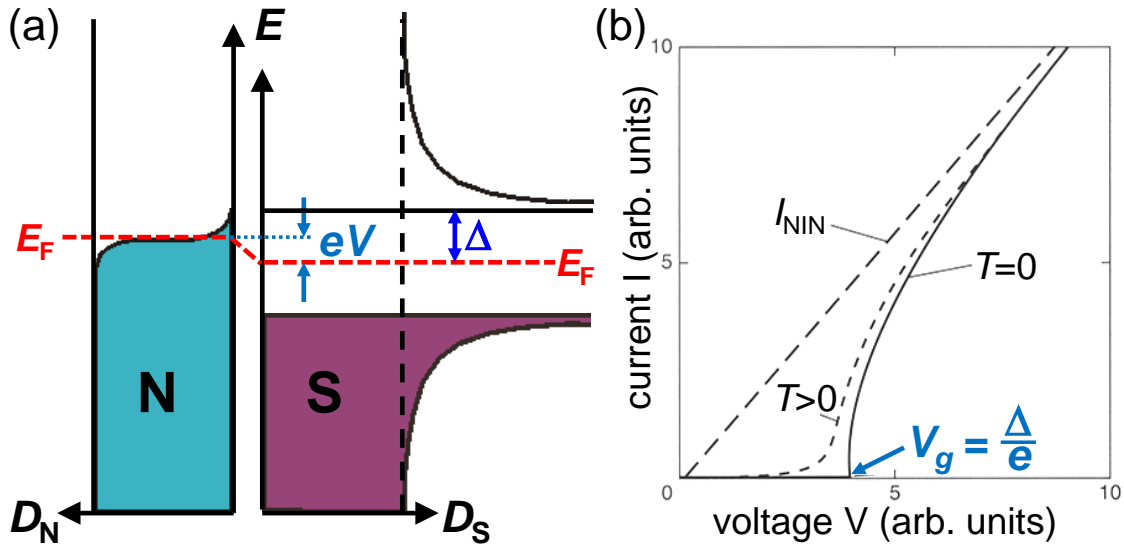


Fig. 4.4: N/I/S junction: (a) density of states diagram for the case of an applied voltage $V < \Delta/e$. (b) IV characteristics at $T = 0$ and $T > 0$. The dashed curve is the tunneling characteristics for the case that both electrodes are normal conducting (NIN junction). For large voltages, the NIS characteristics approach asymptotically the NIN characteristics.

With the assumption that the density of states of the normal conductor $D_N(\epsilon) = D_N(0) = \text{const}$ (with $\epsilon \equiv E - E_F$), one can take this out of the integral, and the tunneling current follows as

$$I \propto D_N(0) \int_{-\infty}^{+\infty} D_S(\epsilon) [f(\epsilon - eV) - f(\epsilon)] d\epsilon \quad . \quad (4.18)$$

For the differential conductance $G \equiv (\partial I / \partial V)$ follows then

$$G_{SN}(V) \propto \int_{-\infty}^{+\infty} D_S(\epsilon) K(\epsilon - eV) d\epsilon \quad . \quad (4.19)$$

Hence, G_{SN} is the convolution of the superconducting density of states $D_S(\epsilon)$ with $K(\epsilon - eV)$, i.e., the derivative of the Fermi distribution $f(\epsilon - eV)$ with respect to V

$$K = e\beta \frac{\exp[\beta(\epsilon - eV)]}{\{1 + \exp[\beta(\epsilon - eV)]\}^2} \quad \text{with } \beta \equiv 1/k_B T . \quad (4.20)$$

Figure 4.5 shows the density of states $D_S(\epsilon)$, the function $K(\epsilon)$ and the tunneling conductance $G_{SN}(V)$, as calculated from Eq. (4.19):

The function $K(\epsilon)$ has a maximum at $\epsilon = eV$ and becomes a delta function in the limit $T \rightarrow 0$. In this limit, $G_{SN}(V)$ has the same functional shape as $D_S(\epsilon)$. This means that the measurement of the tunneling characteristics yields at low temperatures just the density of states of the superconductor.

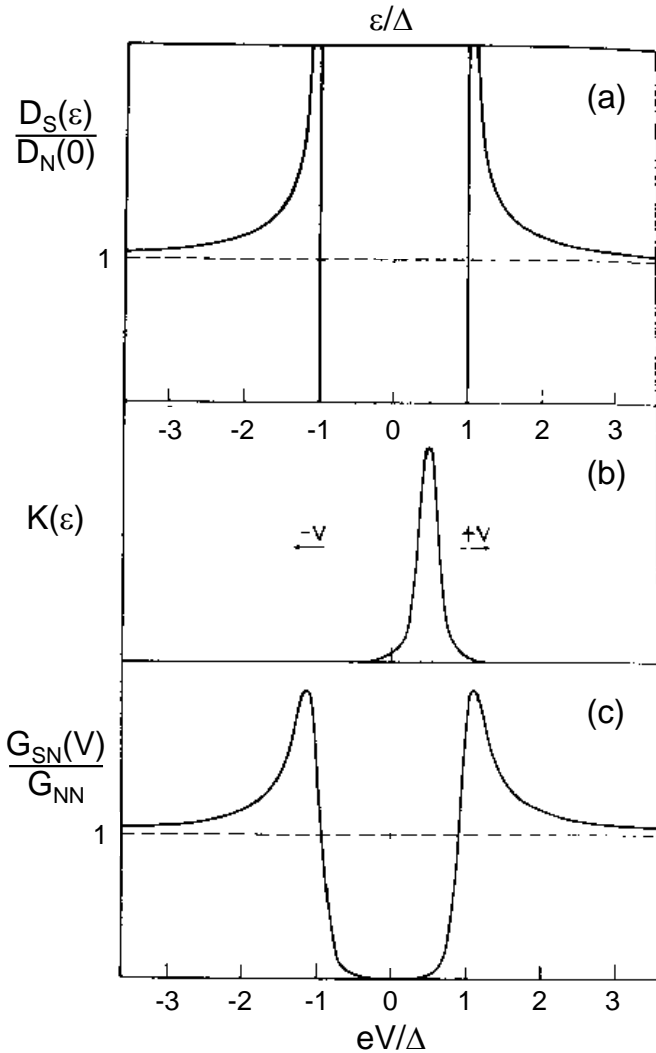


Fig. 4.5: N/I/S-junction: (a) density of states $D_S(\epsilon)$ according to Eq. (4.17); (b) function $K(\epsilon)$ for $eV \approx \Delta/2$ according to Eq. (4.20); (c) tunneling conductance $G_{SN}(V)$ according to Eq. (4.19) [after R. Meservey, P. M. Tedrow, Physics Reports **238**, 173 (1994)].

The analysis described above goes back to Giaever and Megerle⁹. This has been extended to superconductor/insulator/ferromagnet (SIF) junctions. This allows for the determination of the spin polarization of ferromagnets.¹⁰

⁹I. Giaever, K. Megerle, Phys. Rev. **122**, 1101 (1961)

¹⁰P.M. Tedrow, R. Meservey, Phys. Rev. Lett. **26**, 192 (1971)

SIS junction

The case of quasiparticle tunneling in superconductor/insulator/superconductor (SIS) junctions is shown in Fig. 4.6, for two superconductors with different energy gap $\Delta_I < \Delta_{II}$.

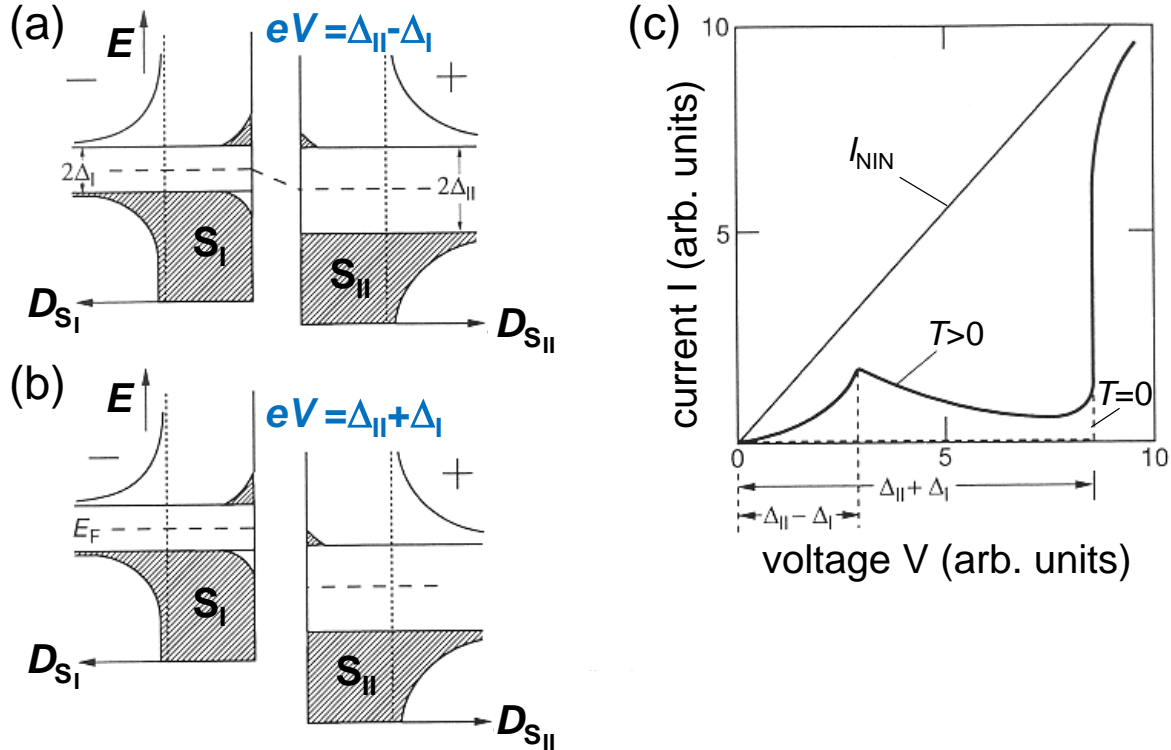


Fig. 4.6: SIS junction with energy gap $\Delta_I < \Delta_{II}$: (a), (b) density of states diagrams for $0 < T < T_c$ at (a) $eV = \Delta_{II} - \Delta_I$ and (b) $eV = \Delta_{II} + \Delta_I$. (c) current-voltage characteristics for $0 < T < T_c$ (solid line) and for $T = 0$ (dashed line) [adapted from W. Buckel, R. Kleiner, *Supraleitung*, Wiley-VCH Weinheim, 7. Aufl. (2013); Abb.3.15].

The thermal occupation of excited states above the energy gap leads to a local maximum in the $I(V)$ characteristics at $V = (\Delta_{II} - \Delta_I)/e$, as under this condition the thermally excited (occupied) states in S_I are facing a high density of unoccupied states in S_{II} . This local maximum disappears in the case $T \rightarrow 0$, as there will be no thermally excited quasiparticles available.

With further increasing voltage, the tunneling current decreases again, until a steep rise in the tunneling current appears at the gap voltage $V_g = (\Delta_{II} + \Delta_I)/e$. Here, a high density of occupied states (below the energy gap) in S_I is facing a high density of unoccupied states in S_{II} . Note that if the two electrodes are from the same material (i.e. $\Delta_1 = \Delta_2 = \Delta$) the gap voltage of the SIS tunnel junction is $V_g = 2\Delta/e$, i.e. a factor of two larger than V_g of the NIS tunnel junction.¹¹

¹¹For his contributions to quasiparticle tunneling in NIS and SIS junctions, and in particular for the related clear experimental proof of the existence of an energy gap in the quasiparticle spectrum of superconductors, as predicted by the BCS theory, Ivar Giaever received in 1973 the Nobel prize in physics, together with Leo Esaki and Brian Josephson.

4.2 Josephson effects & SQUIDs

4.2.1 Weak superconductivity: Josephson effects

So far, for SIS-junctions we have only considered the tunneling of unpaired electrons (quasiparticles). In the following, we will discuss the tunneling of Cooper pairs between two superconducting electrodes. This effect has been predicted by Brian D. Josephson in a theoretical work in the year 1962¹², and it has been confirmed experimentally one year later by Anderson and Rowell¹³.

Starting point is the fact that all the electric charge carriers (Cooper pairs) in a superconductor can be described by a single macroscopic wave function $\Psi = \Psi_0 e^{i\varphi}$, with amplitude Ψ_0 and phase φ . The squared modulus of the amplitude, $|\Psi_0|^2$, is proportional to the Cooper pair density n_s . According to the 2. Ginzburg Landau equation, the Cooper pair current (and hence the momentum, or the velocity of the Cooper pairs) is related to a gradient of the phase. For the supercurrent density j_s one finds the relation

$$\mathbf{j}_s = \frac{q_s n_s}{m_s} (\hbar \nabla \varphi - q_s \mathbf{A}) . \quad (4.21)$$

Here, \mathbf{A} is the vector potential, which is via $\nabla \times \mathbf{A} = \mathbf{B}$ connected to the magnetic induction (flux density) \mathbf{B} ; $q_s = 2e$ is the charge and $m_s = 2m_e$ is the mass of the Cooper pairs. With the definition of the **gauge-invariant phase gradient**

$$\nabla \phi \equiv \nabla \varphi - \frac{q_s}{\hbar} \mathbf{A} \quad (4.22)$$

one has $\mathbf{j}_s = \frac{q_s n_s}{m_s} \hbar \nabla \phi$, i.e. $\mathbf{j}_s \propto n_s \nabla \phi$. By integration of (4.22) one obtains the **gauge-invariant phase**

$$\phi(\mathbf{r}) = \varphi(\mathbf{r}) - \frac{q_s}{\hbar} \int_{\mathbf{r}_0}^{\mathbf{r}} \mathbf{A} d\mathbf{r} . \quad (4.23)$$

We consider now two superconductors S_1 and S_2 , with the macroscopic wave functions $\Psi_1 = \Psi_{0,1} \cdot e^{i\varphi_1}$ and $\Psi_2 = \Psi_{0,2} \cdot e^{i\varphi_2}$.

Question: what happens when the two superconductors are coupled via a weak link ?
→ is there a relation between the wave functions Ψ_i (phases φ_i) and current I_s across the weak link (e.g. insulating tunnel barrier; see Fig. 4.7) ?

¹²B. D. Josephson, *Possible new effects in superconductive tunneling*, Phys. Lett. **1**, 251 (1962). Josephson received in the year 1971 the Nobel prize in physics for his theoretical work on the Cooper pair tunneling, which is also denoted as the Josephson effect.

¹³P. W. Anderson and J. M. Rowell, *Possible observation of the Josephson superconducting tunneling effect*, Phys. Rev. Lett. **10**, 230 (1963).

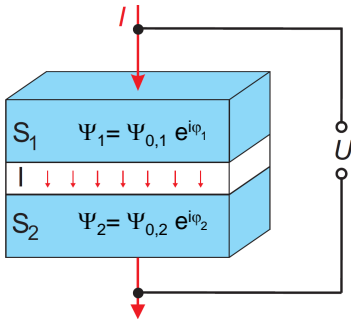


Fig. 4.7: Schematic representation of a Josephson tunnel junction. The superconducting electrodes (S_1, S_2) are blue and the insulating layer (I) is white. One injects a current I , and detects the voltage U across the junction.

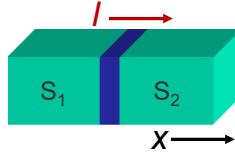
weak, but finite coupling

→ Overlap of the wave functions Ψ_i

→ **Supercurrent through the barrier**

S/barrier/S configuration:

(barrier plane $\perp x$;
cross section $A_J = \text{const}$)



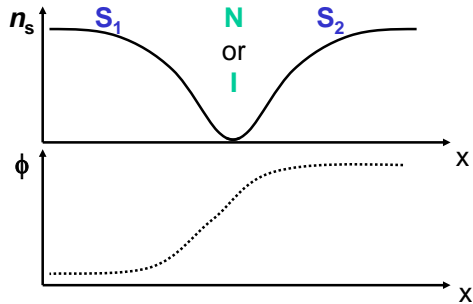
Upon injection of a constant current I in this device (here: I in x -direction), the supercurrent density in x -direction has to be constant:

$$j_s(x) = I/A_J = \text{const}$$

. Hence, because of $\vec{j}_s \propto n_s \vec{\nabla} \phi$ from (4.21)

$$n_s(x) \cdot \frac{\partial \phi}{\partial x}(x) = \text{const} \quad . \quad (4.24)$$

A change in the charge carrier density n_s at the weak link is compensated by an according change in $\partial \phi / \partial x$.



In the barrier region (normal conductor N or insulator I):

n_s small [‘Dip’ in $n_s(x)$]
 $\Rightarrow \partial \phi / \partial x$ large [‘Peak’ in $\partial \phi / \partial x(x)$]
 $\Rightarrow \phi(x)$ makes a step

For a very thin barrier with $n_s \rightarrow 0$
 $\Rightarrow \phi(x)$ makes a ‘jump’ at the barrier

⇒ Weak link characterized by

$$\begin{aligned} \text{phase difference } \delta &\equiv \phi_2 - \phi_1 \\ &= \varphi_2 - \varphi_1 - \frac{q_s}{\hbar} \int_1^2 A_x dx \end{aligned} \quad (4.25)$$

→ analogous to $j_s \propto \nabla \phi$ in (4.21) for the current density in a homogeneous superconductor, the **supercurrent density** across the junction becomes a **function of the phase difference** $j_s = j_s(\delta)$.

Question: what is the functional relation $j_s(\delta)$?

→ 'Motivation' for $j_s(\delta)$ from simple considerations:

- Phases ϕ_i are unique modulo 2π

$$\Rightarrow j_s = \text{periodic function of } \delta$$

$$j_s = \sum_n j_{0n} \sin n\delta + \sum_n \tilde{j}_{0n} \cos n\delta \quad (n = 1, 2, \dots)$$

- time reversal invariance

$$\left. \begin{array}{l} j_s \rightarrow -j_s \text{ upon time reversal} \\ \text{phase } \delta \rightarrow -\delta \text{ upon time reversal } (\psi \propto e^{-i\omega t}) \end{array} \right\} \Rightarrow j_s(\delta) = -j_s(-\delta)$$

$$\Rightarrow \text{cos-terms can be excluded:} \quad j_s = \sum_n j_{0n} \sin n\delta$$

- Very often: fast convergence $j_{0n} \ll j_{01}$ for $n > 1$

$$\Rightarrow j_s = j_0 \sin \delta \quad \text{1. Josephson equation} \quad (4.26)$$

Supercurrent across barrier = "Josephson current"

Corresponds in a SIS tunnel junction to the **tunneling of Cooper pairs** through an insulating barrier. This case has been considered by Brian D. Josephson for his derivation of the Josephson equations.¹⁴

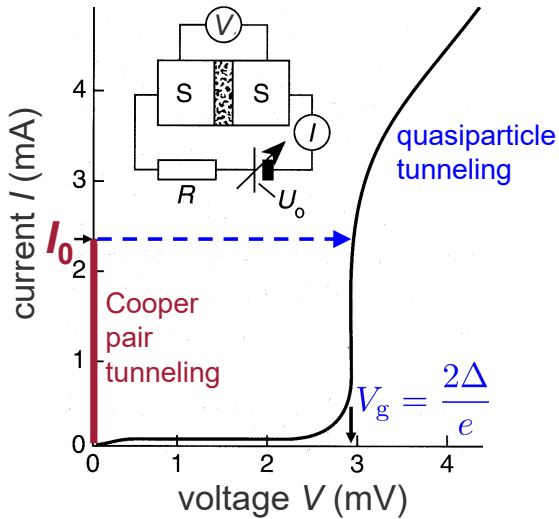
From the consideration of the **change of δ in time**, Josephson obtained the connection of $\frac{\partial \delta}{\partial t} \equiv \dot{\delta}$ with the voltage drop U across the barrier (with the magnetic flux quantum $\Phi_0 \equiv h/2e$)

$$U = \frac{\hbar}{2e} \dot{\delta} = \frac{\Phi_0}{2\pi} \dot{\delta} \quad \text{2. Josephson equation} \quad (4.27)$$

¹⁴A derivation suggested by Feynman, based on the time-dependent Schrödinger equations for two weakly coupled quantum mechanical systems, can be found in W. Buckel, R. Kleiner, *Supraleitung*, Wiley-VCH Weinheim, 6. Aufl. (2004); Kap.1.5.1.

Consequences from the Josephson equations

- assume $U = 0 \Rightarrow \delta = \text{const} = \delta_0 \Rightarrow j_s = j_0 \sin \delta_0$
maximum value: $\sin \delta_0 = 1 \Rightarrow j_{s,\max} = j_0$
→ supercurrent; critical current density $j_0 \ll j_{c,\text{pair breaking}}$.
→ "weak superconductivity"



Example:

Nb/Al-AlO_x/Nb tunnel junctions depending on barrier thickness
 $j_0 \sim (10 \text{ A} \dots 10 \text{ kA})/\text{cm}^2$
 $= (1 \mu\text{A} \dots 1 \text{ mA})/(10 \mu\text{m}^2)$
(at $T = 4.2 \text{ K}$)

Fig. 4.8: Current-voltage characteristics of a Josephson tunnel junction from identical superconductors [adapted from W. Buckel, *Supraleitung*, VCH Weinheim, 5. Aufl. (1994); Abb.37].

- assume $U = \text{const.} \neq 0 \rightarrow$ integration of the 2. Josephson Eq. (4.27):

$$\Rightarrow \delta(t) = \delta_0 + \frac{2\pi}{\Phi_0} U \cdot t \quad (4.28)$$

i.e. δ grows linearly in time t ; inserted into the 1. Josephson Eq. (4.26):

$$j_s = j_0 \sin[\delta_0 + \omega_J t] \quad \text{with} \quad \omega_J = \frac{2\pi}{\Phi_0} U \quad (4.29)$$

⇒ Cooper pair alternating current with the Josephson frequency

$$f_J \equiv \frac{\omega_J}{2\pi} = \frac{U}{\Phi_0} = \frac{2e}{h} \cdot U \approx 483.6 \frac{\text{GHz}}{\text{mV}} \cdot U \quad (4.30)$$

→ voltage-controllable high-frequency source

→ proportionality constant $\Phi_0 \equiv h/2e \rightarrow$ fundamental physical constant

→ effect is used for the definition of the Volt

Compare to: Quantum-Hall effect: $R_H = \frac{1}{n} \underbrace{\frac{h}{e^2}}_{\approx 25.8 \text{ k}\Omega} \quad (\text{defines } \Omega)$

Interpretation of the Josephson (alternating) currents as quantum interference:

$U \neq 0 \rightarrow$ phases of the macroscopic wave functions $\Psi_i = \Psi_{0,i} e^{i\varphi_i}$
in both superconductors ($i = 1, 2$) "run against each other".

Josephson alternating current \Leftrightarrow interference of these waves in time

Types of Josephson junctions (JJs)

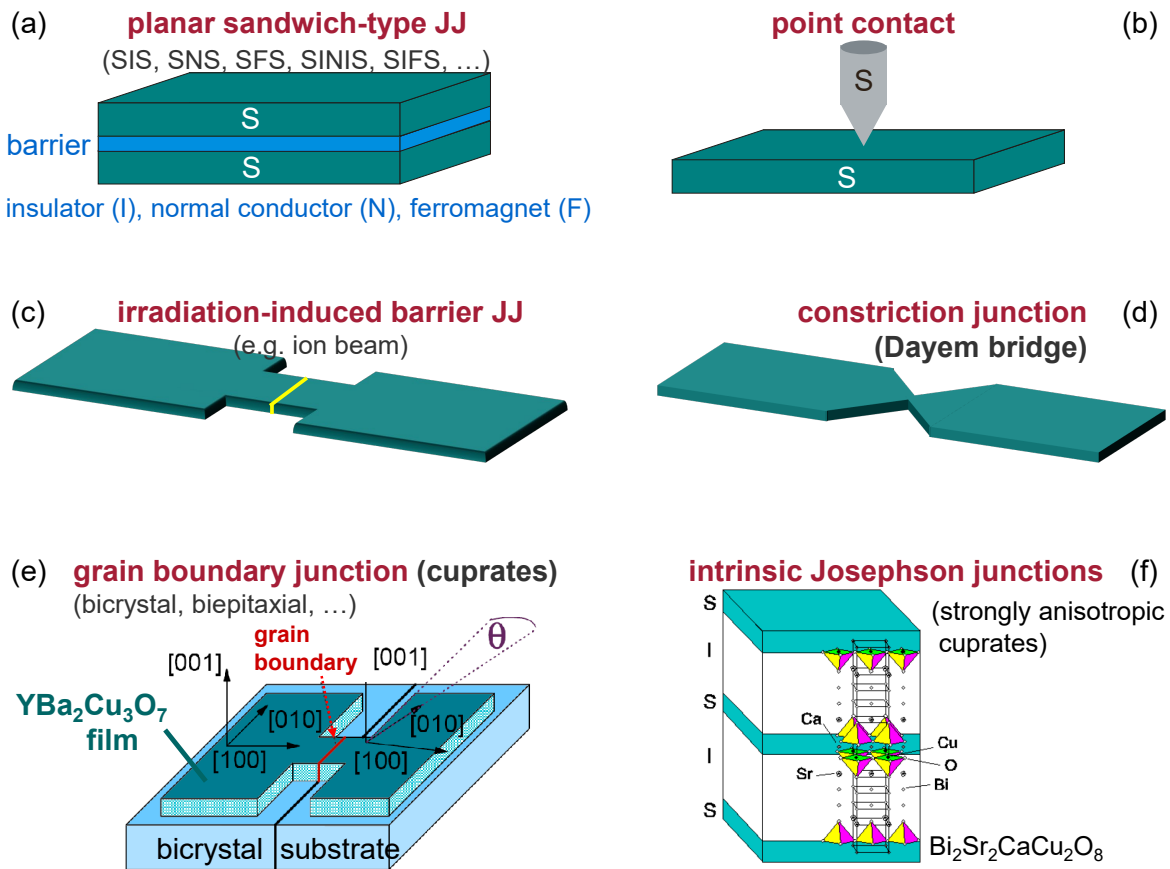


Fig. 4.9: Different types of Josephson junctions: (a) planar sandwich-type JJ. The barrier can be an insulator (I; often a 1–2 nm thick oxide layer as tunnel barrier), normal metal (N) or ferromagnet (F) or a combination of those (e.g. SINIS or SIFS). (b) point contact: Tip is pressed onto surface; pressure determines junction area and hence the junction properties. (c) thin-film micro/nano bridge, where a Josephson barrier is used by damaging (e.g. by ion irradiation) locally the superconducting material. (d) Dayem bridge: Very small cross section (< 100 nm) limits exchange of Cooper pairs. (e) grain boundary (GB) junction: In cuprate superconductors (e.g. $\text{YBa}_2\text{Cu}_3\text{O}_7$ (YBCO)), grain boundaries with misorientation angle $\Theta \gtrsim 10^\circ$ act as weak links (forming ~ 1 -nm-thick insulating tunnel barriers). In the case of bicrystal GB junctions (drawn here), the GB in the substrate is transferred by epitaxial growth into the superconducting film. (f) Intrinsic Josephson junctions [drawing provided by Reinhold Kleiner]: In strongly anisotropic cuprate superconductors (e.g. $\text{Bi}_2\text{Sr}_2\text{CaCu}_2\text{O}_8$ (BSCCO-2212)), already the crystal structure leads to Josephson behavior. The superconductivity is localized within only ~ 0.3 nm thick layers of copper oxide. These layers are separated by layers of Bismuth- and Strontiumoxide. Therefore, single crystals form natural stacks of SISIS... layers, also called intrinsic Josephson junctions. A single crystal with a thickness of only $1\ \mu\text{m}$ (in c -axis direction) contains approximately 670 intrinsic Josephson junctions.

most frequently used:

- conventional superconductors: $\text{Nb}/\text{Al}-\text{AlO}_x/\text{Nb}$ (for $T < 9$ K)
- high- T_c -superconductors: grain boundary junctions or intrinsic Josephson junctions¹⁵

¹⁵R. Kleiner, P. Müller, Phys. Rev. B **49**, 1327 (1994)]

current-voltage characteristics of Josephson junctions

Now, we ask for the relation between the current I through the Josephson junction and the voltage U across the junction. For many types of junctions, the *resistively and capacitively shunted junction model = RCSJ model*¹⁶ gives a very good description. Here, we consider **four terms** which contribute to **the current through the junction**:

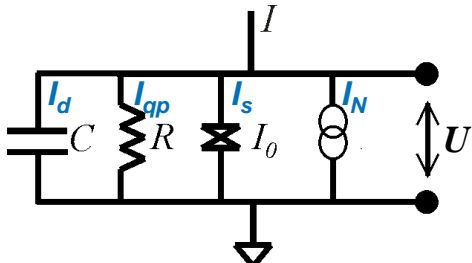


Fig. 4.10: Equivalent circuit of a Josephson junction in the RCSJ model.

- **Josephson current:** $I_s = I_0 \sin \delta$
- **displacement current through the capacitance** C of the junction, which flows if there is a time-dependent voltage U : $I_d = C \dot{U}$
- **dissipative current contribution from the quasiparticles**, or current, which flows through a frequently used parallel resistance R : $I_{qp} = U/R$
- **noise current** $I_N(t)$, due to thermal noise¹⁷ in the resistance R at finite temperature T

According to **Kirchhoff's laws** this yields for the total current I through the junction:

$$I + I_N(t) = I_0 \sin \delta + \frac{U}{R} + C \dot{U} \quad (4.31)$$

Using the 2. Josephson equation $U = (\Phi_0/2\pi) \cdot \dot{\delta}$, we then obtain a **differential equation for the phase difference** across the Josephson junction

$$I + I_N(t) = I_0 \sin \delta + \frac{\Phi_0}{2\pi R} \dot{\delta} + \frac{\Phi_0 C}{2\pi} \ddot{\delta} \quad (4.32)$$

In the case of a finite voltage $U \neq 0$, alternating Josephson currents are flowing

\Rightarrow also the dissipative current $I_{qp}(t)$ oscillates

\Rightarrow high-frequency voltage $U(t)$ with dc voltage contribution

$$V \equiv \langle U \rangle = \frac{1}{T} \int_0^T dt U(t) \quad (4.33)$$

The solution of the differential equation (4.32) for a given total current I yields $\delta(t) \Rightarrow U(t) \Rightarrow V$ and, hence, also the experimentally easily accessible (dc) **current voltage characteristics** $I(V)$.

¹⁶W. C. Stewart, *Current-voltage characteristics of Josephson junctions*, Appl. Phys. Lett. **12**, 277 (1968); D. E. McCumber, *Effect of ac impedance on dc voltage-current characteristics of Josephson junctions*, J. Appl. Phys. **39**, 3113 (1968).

¹⁷This is also called Nyquist- or Johnson noise; the noise power of I_N scales as $k_B T / R$.

Analogous system: point-like particle in the tilted washboard potential

In a very illustrative analogy to a mechanical system, the equation (4.32) for the phase difference δ describes the motion of a particle in a 1-dimensional potential along the coordinate δ .

In order to show this, we rearrange equation (4.32)

$$\frac{\Phi_0}{2\pi} C \ddot{\delta} + \frac{\Phi_0}{2\pi} \frac{1}{R} \dot{\delta} = -I_0 \sin \delta + (I + I_N) \equiv -\frac{2\pi}{\Phi_0} \frac{\partial U_J}{\partial \delta} , \quad (4.34)$$

Here, we defined the so-called *tilted washboard potential* as

$$U_J \equiv \frac{\Phi_0}{2\pi} \{I_0(1 - \cos \delta) - (I + I_N)\delta\} . \quad (4.35)$$

The amplitude of the potential is given by the *Josephson coupling energy*

$$E_J \equiv \frac{I_0 \Phi_0}{2\pi} . \quad (4.36)$$

With normalization of U_J to E_J , the equation above yields

$$u_J \equiv \frac{U_J}{E_J} = 1 - \cos \delta - (i + i_N)\delta \quad \text{with} \quad i \equiv I/I_0, i_N \equiv I_N/I_0 . \quad (4.37)$$

Hence, the equation of motion (4.34) for δ is equivalent to the equation of motion

$$m \ddot{x} + \xi \dot{x} = -\frac{\partial W(x)}{\partial x} + F_d + F_N = -\frac{\partial [W(x) - (F_d + F_N) \cdot x]}{\partial x} \quad (4.38)$$

of a point-like particle with mass m and friction coefficient ξ , which moves in space along the coordinate x in a potential $W(x)$ under the action of an external driving force F_d and a thermal noise force F_N .

One can combine the driving forces $F = F_d + F_N$ with the potential W , and arrives then at the potential

$$U_m(F, x) \equiv W(x) - F \cdot x , \quad (4.39)$$

which is 'tilted' due to the forces.

$$m \ddot{x} + \xi \dot{x} = -\nabla w(x) + F_d(t) + F_N(t) \quad \longleftrightarrow \quad \frac{\Phi_0 C}{2\pi} \ddot{\delta} + \frac{\Phi_0}{2\pi R} \dot{\delta} = -I_0 \sin \delta + I(t) + I_N(t)$$

velocity	\dot{x}	\longleftrightarrow	$\dot{\delta} (\Phi_0/2\pi) = U$	voltage	Comparison of (4.34) with (4.38) yields analogous quantities.
force	F_d, F_N	\longleftrightarrow	I, I_N	current	
friction	ξ	\longleftrightarrow	$1/R$	conductance	
mass	m	\longleftrightarrow	C	capacitance	

static case: $V = 0$

In the current-free state $I = 0$ (without external force) our 'particle' is trapped in one of the minima of the untilted cos-potential. There, it oscillates with the plasma frequency ¹⁸ $\omega_p = \left(\frac{2\pi I_0}{\Phi_0 C}\right)^{1/2}$, and the average voltage (velocity) is zero.

dynamic case: $V \neq 0$

With increasing bias current I , the height of the barrier to the next local minimum decreases. Finally, at $I = I_0$ the local minima disappear, and the 'particle' moves with finite average velocity (Fig. 4.11).

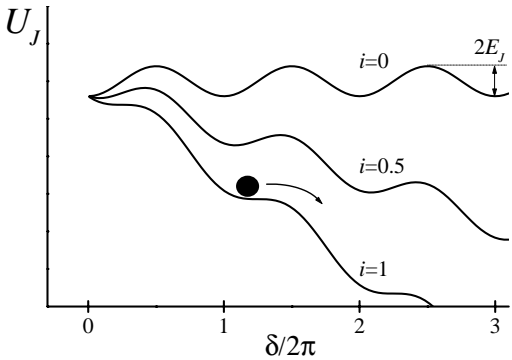


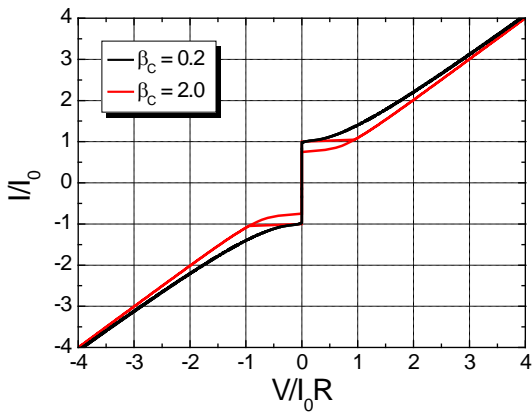
Fig. 4.11: Washboard potential of a Josephson junction in the RCSJ model, with amplitude E_J (coupling energy). The normalized bias current $i = I/I_0$ tilts the potential. At $i = 1$, the local minima disappear.

Effect of damping:

In the **case of strong damping**, the mass of the particle is negligible, i.e. the friction term $\propto \dot{\delta}$ dominates. Upon decreasing back the current, at $I = I_0$ local minima appear again in the washboard potential, and the particle is immediately trapped there
→ **non-hysteretic IV-characteristics (IVC)**

In the **case of weak damping**, the mass of the particle plays a key role. Upon decreasing back the current, even in the case $I < I_0$ (local minima/maxima have formed) the particle can still continue to move due to inertia. In this case, the Josephson junction remains in the state $V \neq 0$, down to a value ("retrapping current") $I_r < I_0$
→ **hysteretic IVC**; is described by the *Stewart-McCumber-Parameter* β_C in the normalized equation of motion (currents $i \equiv I/I_0$, $i_N \equiv I_N/I_0$; time $\tilde{t} \equiv t\omega_c$, with $\omega_c \equiv \frac{2\pi}{\Phi_0} I_0 R$)

$$\beta_C \ddot{\delta} + \dot{\delta} + \sin \delta = i + i_N \quad \text{with} \quad \beta_C \equiv \left(\frac{\omega_c}{\omega_p}\right)^2 = \frac{2\pi}{\Phi_0} I_0 R^2 C \quad (4.40)$$



- overdamped $\beta_C \lesssim 1$ → non-hysteretic IVC
- underdamped $\beta_C \gtrsim 1$ → hysteretic IVC

Fig. 4.12: Current-voltage characteristics in the RCSJ model, calculated for different damping (different values for β_C).

¹⁸Derivation by solving (4.32) for the case $I = 0$, $I_N = 0$ ($T = 0$), $1/R = 0$.

Dynamics under the influence of an alternating current

Consider the case of a driving current $I_{\text{tot}} = I + I_{\text{ac}} \sin \omega_{\text{ac}} t$ with dc component I and ac current with amplitude I_{ac} and frequency $f_{\text{ac}} = \omega_{\text{ac}}/2\pi$.

experimental observation:

Appearance of regimes of constant voltage in the IVC = **Shapiro steps**

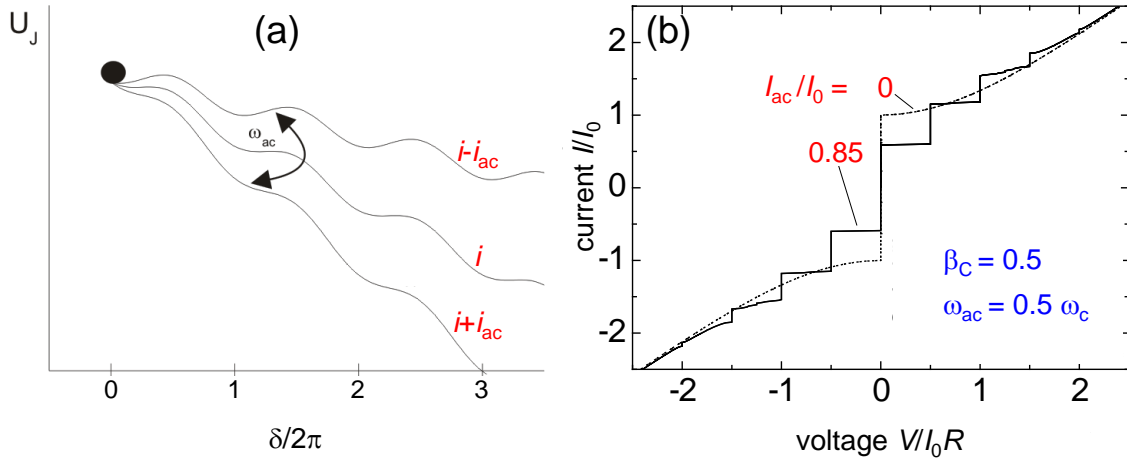


Fig. 4.13: (a) Illustration of the generation of Shapiro steps within the washboard potential of a Josephson junction in the RCSJ model. The potential – tilted by the normalized dc current i – is in addition periodically tilted, due to microwave irradiation with frequency ω_{ac} . (b) From the RCSJ model calculated current-voltage characteristics of a Josephson junction under microwave irradiation. The dotted line shows the IV characteristics without microwave irradiation.

Illustrative interpretation:

The ac current generates a periodic modulation of the tilt of the potential about a mean tilt angle (given by the dc current).

Under appropriate conditions, the motion of the 'particle' is synchronized with the external excitation:

\Rightarrow change of δ by $n \cdot 2\pi$ per excitation period $T_{\text{ac}} = 2\pi/\omega_{\text{ac}}$.

\Rightarrow velocity $\dot{\delta} = n \cdot 2\pi/T_{\text{ac}} = n \cdot \omega_{\text{ac}}$

This synchronization is stable within certain regions of the tilt angle (current intervals). There, the average velocity (dc voltage) is only given by the frequency of the ac drive – independent of the exact value of the average tilt angle (dc current). This leads to the appearance of current steps of constant voltage:

$$V_n = \frac{\Phi_0}{2\pi} \dot{\delta} = n \frac{\Phi_0}{2\pi} \omega_{\text{ac}} = n \cdot V_1 \quad \text{with} \quad V_1 \equiv \Phi_0 \cdot f_{\text{ac}} \approx \frac{1 \text{ mV}}{483.6 \text{ GHz}} \cdot f_{\text{ac}} \quad (4.41)$$

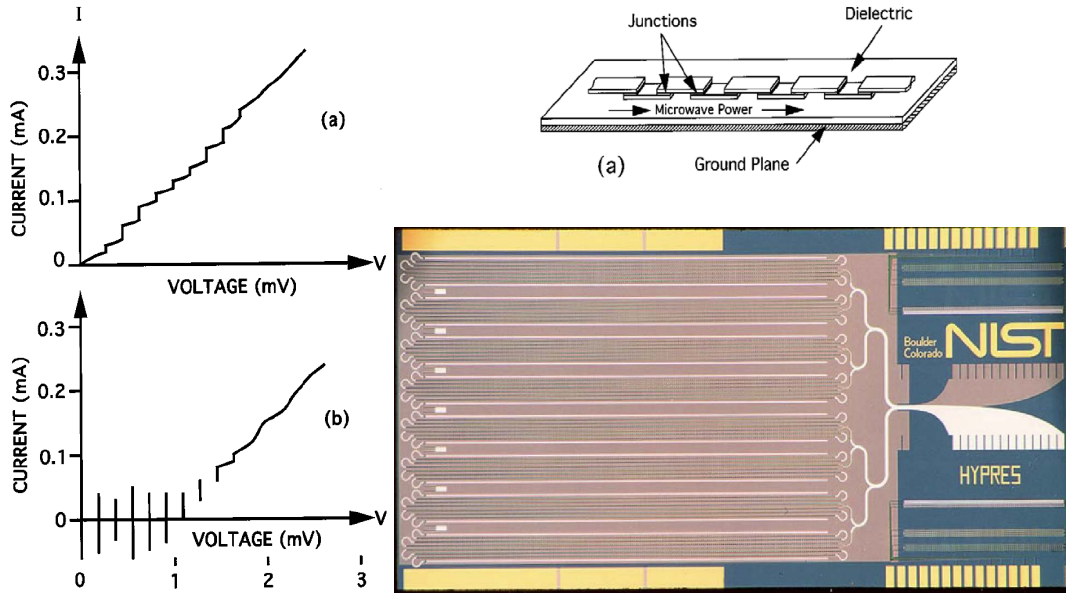
→ Application: voltage normal !

Definition of the SI unit Volt via the Josephson effect

Josephson normal: voltage standard

irradiation of microwaves on Josephson junctions
(typically: $f = 70 \text{ GHz} \rightarrow n \cdot 0.144 \text{ mV}$)

$$V = n\Phi_0 f$$



reproducible voltages with relative uncertainty
 $< 1 : 10^{10}$, corresponds to 1 nV at 10 V)

Fig. 4.14: On the Josephson voltage normal.

Josephson junction in a magnetic field

Consider a Josephson junction in an external magnetic field H in the plane of the barrier ((x, y) -plane) and current I perpendicular to it (along \hat{e}_z).

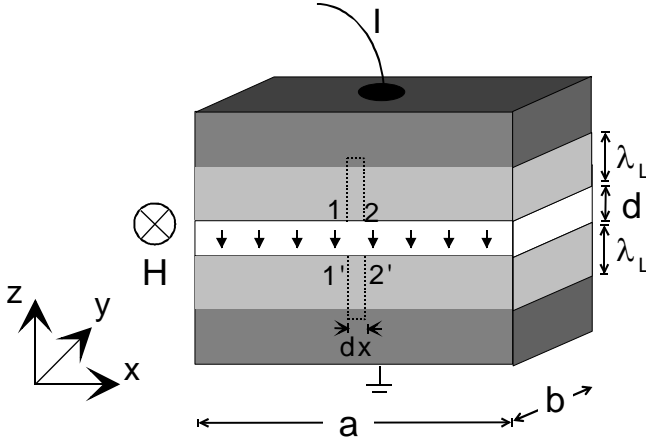


Fig. 4.15: Geometry of a Josephson junction in an external magnetic field H ; d : barrier thickness; a : length of the junction along x -direction ($\perp H$). The light-grey area is penetrated by the magnetic field. The dashed line indicates the integration path for the derivation of Eq. (4.43).

The magnetic field shall penetrate the barrier homogeneously (along x -direction). This is the case when the junction length a is sufficiently small, so the self-field of the currents is negligible (= limit of short junction¹⁹).

The thickness of the superconducting electrodes shall be $\gtrsim 2\lambda_L$ (λ_L : London penetration depth)

→ the magnetic field penetrates $\sim \lambda_L$ in the electrodes (along z -direction).

→ magnetic flux through the junction, with $B = \mu_0 H$:

$$\Phi_J = B \cdot (2\lambda_L + d) \cdot a = B \cdot d_{\text{eff}} \cdot a , \quad (4.42)$$

with the effective magnetic thickness of the junction $d_{\text{eff}} \equiv 2\lambda_L + d$

Relation between phase difference δ and magnetic induction (flux density) B

Analogous to the derivation of flux quantization in a superconductor:

Integration of the phase gradient $\vec{\nabla}\varphi$ along the dashed line in Fig. 4.15 yields

$$\frac{\partial \delta}{\partial x} = \frac{2\pi}{\Phi_0} B d_{\text{eff}} \quad (4.43)$$

This means, that the phase difference along the junction grows linearly (slope determined by B). Integration along x

$$\Rightarrow \delta(x) = \delta(0) + \frac{2\pi}{\Phi_0} B d_{\text{eff}} \cdot x \quad (4.44)$$

and inserted into the 1. Josephson equation (for the current density, i.e., current per junction area $A_J = ab$, with size b of the junction in y -direction) yields

$$j_s(x) = \underbrace{j_0}_{=I_0/A_J} \sin \left[\delta(0) + \frac{2\pi}{\Phi_0} B d_{\text{eff}} \cdot x \right] \quad (4.45)$$

⇒ Josephson current density $j_s(x)$ oscillates along the junction. The wavelength of the oscillation depends on the magnetic flux $\Phi_J = B d_{\text{eff}} a$ in the junction.

¹⁹If $a \lesssim 4\lambda_J$ with the Josephson penetration depth $\lambda_J \equiv [\Phi_0/(2\pi\mu_0 d_{\text{eff}} j_0)]^{1/2}$

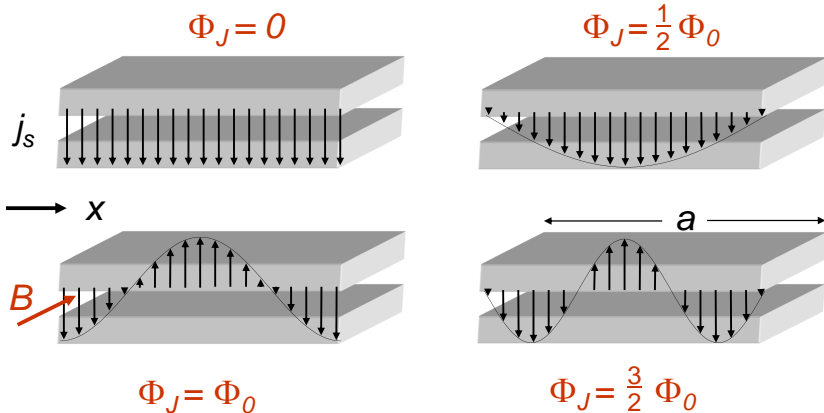


Fig. 4.16: Current density distribution in a short Josephson junction in a magnetic field. The starting value of the phase difference $\delta(x = 0) \equiv \delta_0$ is always chosen such that the Josephson current becomes maximum.

Total supercurrent through the junction \rightarrow integrate $j_s(x)$ over the junction area:

$$\begin{aligned} I_s &= \int_0^b dy \int_0^a dx j_0 \sin \delta(x) = -j_0 \cdot b \cdot \left. \frac{\cos \left(\delta_0 + \frac{2\pi}{\Phi_0} Bd_{\text{eff}} x \right)}{\left(\frac{2\pi}{\Phi_0} Bd_{\text{eff}} \right)} \right|_0^a \\ &= \underbrace{j_0 \cdot b \cdot a}_{I_0} \cdot \frac{\sin \pi \frac{\Phi_J}{\Phi_0}}{\pi \frac{\Phi_J}{\Phi_0}} \cdot \sin(\delta_0 + \pi \frac{\Phi_J}{\Phi_0}) \quad \text{with } \Phi_J = Bd_{\text{eff}}a \end{aligned} \quad (4.46)$$

For given $I_s \Rightarrow \delta_0$ adjusts accordingly

Maximum super current I_c $\rightarrow \sin(\delta_0 + \pi \frac{\Phi_J}{\Phi_0}) \pm 1 \Rightarrow$

$$I_c(\Phi_J) = I_0 \cdot \left| \frac{\sin \pi \frac{\Phi_J}{\Phi_0}}{\pi \frac{\Phi_J}{\Phi_0}} \right| \quad (4.47)$$

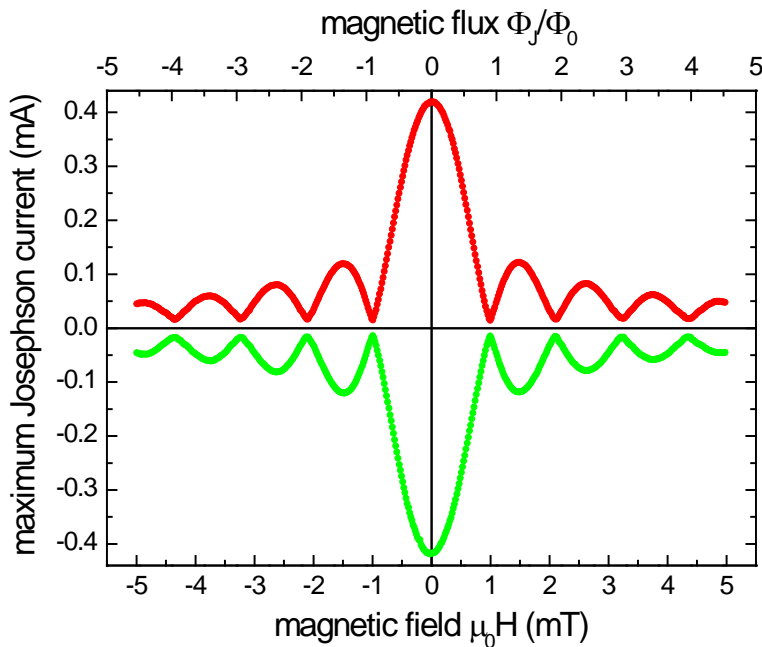


Fig. 4.17: Dependence of the maximum Josephson current on the magnetic field or the normalized magnetic flux in the plane of a Nb/AlO_x/Nb tunnel junction.

\Rightarrow **Fraunhofer pattern** (analogous to diffraction at a single slit in optics).

4.2.2 SQUIDs: Superconducting quantum interference devices

A. Basic principle

Consists of a superconducting loop (mostly thin film) with inductance L , which is intersected by one (rf SQUID) or two (dc SQUID) Josephson junctions:²⁰

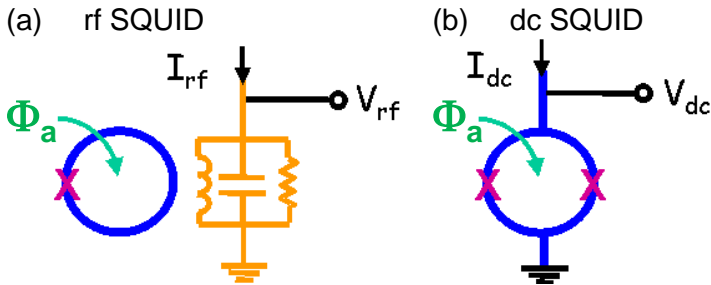


Fig. 4.18: SQUID types: (a) rf SQUID is coupled to a resonant circuit, which is excited with I_{rf} ; output signal: V_{rf} ; (b) dc SQUID is biased at current I_{dc} ; output signal: V_{dc} .

The SQUID combines two basic effects, which rely on the macroscopic phase coherence in a superconductor – the **fluxoid quantization** and the **Josephson effect**

Result:

periodic response to external magnetic flux Φ_a

- in the maximum Josephson current I_c
or
- in the time-averaged voltage V across the Josephson junctions (in the dc SQUID)
or
- in the amplitude V_{rf} of the rf voltage of the resonant circuit (in the rf-SQUID)

with **period = $1\Phi_0$**

⇒ **most sensitive detector for magnetic flux !!**

Typical values for sensitivity (commercial Nb SQUIDs at $T = 4.2\text{ K}$):²¹

$$\text{flux noise: } S_\Phi^{1/2} \approx 1 - 10 \mu\Phi_0 / \sqrt{\text{Hz}}$$

$$\text{magnetic field noise: } S_B^{1/2} \approx 1 - 10 \text{ fT} / \sqrt{\text{Hz}}$$

$$\text{energy resolution: } \epsilon \equiv S_\Phi / 2L \approx 10^{-31} - 10^{-32} \text{ J/Hz} \approx 1000 - 100 \hbar$$

Example:

$$10^{-32} \text{ J} \approx m_e \cdot g \cdot 1 \text{ mm}$$

Difference in potential energy of an electron, which is lifted in the gravitational field of the earth by 1 mm.

²⁰rf = radio frequency; dc = direct current

²¹Here, $S_\Phi(f)$ and $S_B(f)$ are the spectral density of flux noise and field noise power, respectively, of a SQUID. Those quantities generally depend on the measurement frequency f , i.e. $S_\Phi^{1/2}$ and $S_B^{1/2}$ describe the average noise amplitude for magnetic flux or field noise, respectively, per square root of the frequency interval.

B. Basics of the dc SQUID

We consider dc SQUIDs (first realization by Jaklevic *et al.* in the year 1964)²²; in today's applications, those are much more frequently used than rf SQUIDs.

(a) Total flux in the dc SQUID & circulating current

We start with introducing an important relation, which connects the phase differences δ_k across the two Josephson junctions J_k ($k = 1, 2$) with the magnetic flux through the ring. From the fluxoid quantization (as a consequence of the uniqueness of the superconducting wave function), it follows

$$2\pi n = \oint \vec{\nabla} \varphi d\vec{\ell} , \quad \text{with } n = 0, \pm 1, \pm 2, \dots . \quad (4.48)$$

The analysis of the ring integral, along a path inside the superconducting loop (with Eq. (4.21) for $\vec{\nabla} \varphi$) and across the two Josephson junctions (with Eq. (4.25) for δ), results in²³

$$\delta_2 - \delta_1 + 2\pi n = \frac{2\pi}{\Phi_0} (\underbrace{\Phi_a + LJ}_{\equiv \Phi_T}) . \quad (4.49)$$

Here, the *total flux* Φ_T in the SQUID is composed of the externally applied flux Φ_a and the flux which is generated due to an induced circulating current J (through the loop inductance L).

Definition of J :

The dc SQUID is biased at current I ; this splits into the currents I_k through the two SQUID arms (see Fig. 4.19), i.e. $I = I_1 + I_2$. Those can be written as

$$I_1 = \frac{I}{2} + J \quad \text{and} \quad I_2 = \frac{I}{2} - J . \quad (4.50)$$

Hence, the current circulating in the SQUID loop is defined as

$$J = \frac{I_1 - I_2}{2} . \quad (4.51)$$

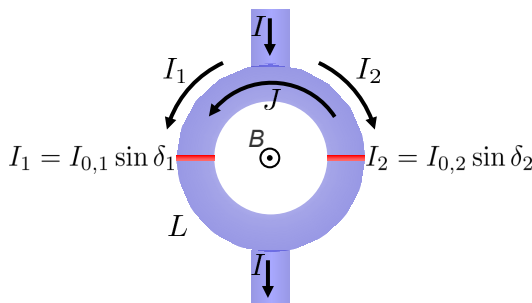


Fig. 4.19: Schematic representation of a dc SQUID, with the Josephson relations for the case of identical junctions, i.e. $I_{0,1} = I_{0,2} = I_0$.

²²R. C. Jaklevic, J. Lambe, A. H. Silver, J. E. Mercereau, Phys. Rev. Lett. **12**, 159 (1964).

²³For a derivation see e.g. Appendix A1 in *The SQUID Handbook, vol.I*, J. Clarke, A. I. Braginskik (eds.), Wiley-VCH (2004).

(b) dc SQUID – static case

In order to understand the working principle of a dc SQUID – i.e. the periodic modulation with the external magnetic flux Φ_a – we consider first the *static case* ($V = 0$), i.e. we ask for the maximum super current (critical current) I_c of the SQUID and for its dependence $I_c(\Phi_a)$.

The currents I_1 and I_2 are flowing through the left (1) and right (2) SQUID arm, respectively, i.e. each across the corresponding junction J1 or J2 (Fig. 4.19). According to the 1. Josephson relation it follows

$$I_1 = I_0 \sin \delta_1 \quad \text{and} \quad I_2 = I_0 \sin \delta_2 \quad , \quad (4.52)$$

under the assumption of symmetric junctions, i.e. identical maximum Josephson currents I_0 .

With Kirchhoff's law for the currents it follows²⁴

$$I = I_0(\sin \delta_1 + \sin \delta_2) = 2I_0 \cos\left(\frac{\delta_2 - \delta_1}{2}\right) \cdot \sin\left(\frac{\delta_1 + \delta_2}{2}\right) \quad . \quad (4.53)$$

By inserting the relation for Φ_T from (4.49) into (4.53),²⁵ we obtain

$$I = 2I_0 \cos\left(\frac{\pi\Phi_T}{\Phi_0} - \pi n\right) \cdot \sin\left(\delta_1 + \frac{\pi\Phi_T}{\Phi_0} - \pi n\right) \quad (4.54)$$

$$= 2I_0 \cos\left(\frac{\pi\Phi_T}{\Phi_0}\right) \cdot \sin\left(\delta_1 + \frac{\pi\Phi_T}{\Phi_0}\right) \quad . \quad (4.55)$$

The supercurrent, as given by Eq. (4.55), can now be maximized by variation of the phase difference δ_1 – for a given external magnetic flux Φ_a and by taking into account the relation $\Phi_T = \Phi_a + LJ$.

In general, the total flux Φ_T depends on the external flux Φ_a and on the circulating current J ; the latter again modulates the phase differences across the junctions. Hence, the solution of this problem is not trivial and is done numerically.

For two frequently considered **special cases** one can derive simple analytical results.

Before we do this, we introduce an important quantity, the so-called **screening parameter**

$$\beta_L \equiv \frac{2I_0L}{\Phi_0} \quad ; \quad (4.56)$$

This describes the strength of the maximum possible flux $\Phi_{J,max} = J_{max}L = I_0L$ – generated by J – normalized to half a flux quantum $\Phi_0/2$.

²⁴with $\sin \alpha + \sin \beta = 2 \cos\left(\frac{\beta-\alpha}{2}\right) \cdot \sin\left(\frac{\alpha+\beta}{2}\right)$

²⁵With $\cos(x - \pi n) \cdot \sin(y - \pi n) = (-1)^n \cdot \cos(x) \cdot (-1)^n \cdot \sin(y) = \cos(x) \cdot \sin(y)$

(I) small SQUID inductance – $\beta_L \ll 1$:

i.e., the flux which can be generated by the maximum possible loop current is negligibly small.

$$\Rightarrow \Phi_T \approx \Phi_a$$

Hence, the screening ability of the SQUID loop is negligible (see Fig. 4.20(a)).

Inserting into (4.55) yields

$$I \approx 2I_0 \cos\left(\frac{\pi\Phi_a}{\Phi_0}\right) \cdot \sin\left(\delta_1 + \frac{\pi\Phi_a}{\Phi_0}\right) . \quad (4.57)$$

I becomes maximum when $\sin(\delta_1 + \frac{\pi\Phi_a}{\Phi_0}) = \pm 1$

\Rightarrow critical current of the dc SQUID:

$$I_c \approx 2I_0 \cdot \left| \cos\left(\frac{\pi\Phi_a}{\Phi_0}\right) \right| . \quad (4.58)$$

This relation is analogous to the optical diffraction pattern at the double slit.

This means, the critical current $I_c(\Phi_a)$ modulates from its maximum possible value $2I_0$ down to zero with a period Φ_0 (see Fig. 4.20(b)).

\Rightarrow in the limit $\beta_L \ll 1$, the modulation amplitude is maximum and is $\Delta I_c = 2I_0$.

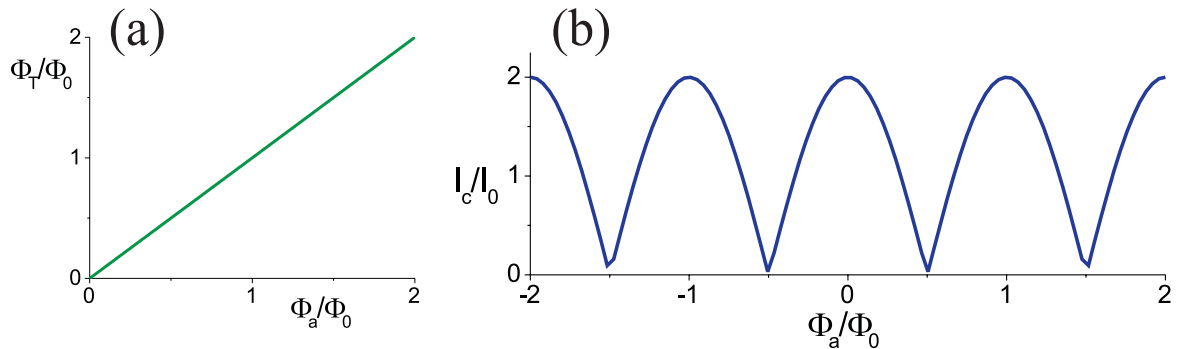


Fig. 4.20: dc SQUID in the limit $\beta_L \ll 1$: (a) Total flux Φ_T vs. external flux Φ_a ; (b) critical current vs. Φ_a .

Appendix:(II) large SQUID inductance – $\beta_L \gg 1$:

In contrast to a closed superconducting loop, the dc SQUID can in the cooled state change its flux state n [see fluxoid quantization (4.48) or (4.49)] upon increasing the external magnetic field. This allows for the minimization of the magnetic energy $LJ^2/2$, which is stored in the loop, by adjusting the flux state n always in such a way that $|J|$ is minimized.

⇒ the flux, which is generated by the circulating current, is at maximum $\Phi_0/2$ ($|L|J \leq \Phi_0/2$).

Hence, in the limit $\beta_L \gg 1$ it follows $L|J| \leq \Phi_0/2 \ll LI_0 \Rightarrow |J| \ll I_0$.

Therefore, the circulating current - independent of the external flux - practically does not affect the phase differences of the junctions, i.e. $\delta_2 - \delta_1 \approx 0$.

Hence, Eq. (4.49) simplifies to

$$\Phi_T = \Phi_a + LJ \approx n\Phi_0 \quad ; \quad (4.59)$$

and hence

$$J \approx -\frac{\Phi_a - n\Phi_0}{L} \quad . \quad (4.60)$$

One sees immediately that, for large L , the circulating current $J \rightarrow 0$

⇒ maximum current ist almost independent of the external flux $I_1 \approx I_2 = I_0$, i.e. the critical current is $I_c \approx 2I_0$ for all Φ_a .

Hence, in contrast to the limit $\beta_L \ll 1$, the modulation of $I_c(\Phi_a)$ is very small.

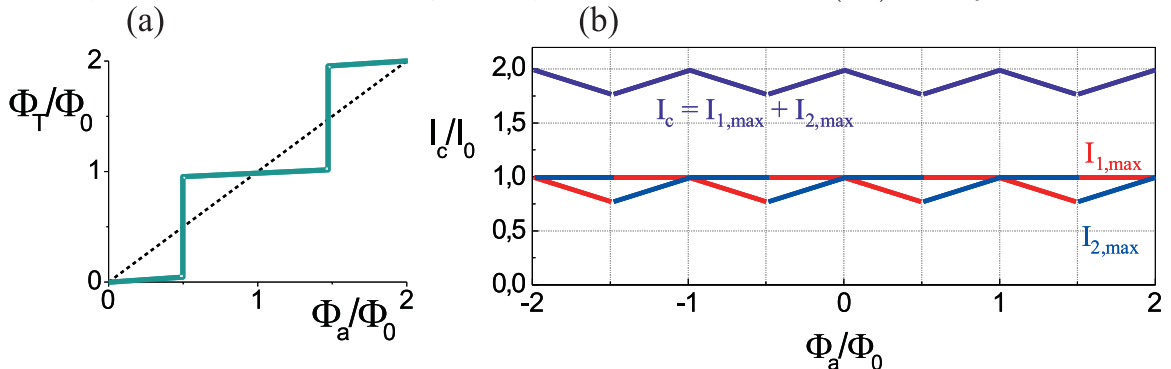


Fig. Z.2: dc SQUID in the limit $\beta_L \gg 1$:

- (a) Total flux Φ_T vs. external flux Φ_a ;
- (b) critical current vs. Φ_a and maximum currents of I_1 and I_2 .

The separate consideration of the effect of J [after Eq. (4.60)] on I_c in intervals $n\Phi_a \leq 0 \leq (n + \frac{1}{2})\Phi_a$, and $(n + \frac{1}{2})\Phi_a \leq 0 \leq (n + 1)\Phi_a$ shows, that always one of the two junctions carries the maximum current I_0 , and the maximum current of the other junction decreases linearly with increasing flux, until at $\Phi_a = (n + \frac{1}{2})\Phi_0$ the flux state and the sign of J change and, hence, the currents through the two junctions are interchanged (see Fig. Z.2).

A relatively simple derivation yields for the maximum change of the critical current

$$\Delta I_c = I_c(\Phi_a = n\Phi_0) - I_c(\Phi_a = [n + \frac{1}{2}]\Phi_0) \approx \frac{\Phi_0}{L} = \frac{2}{\beta_L} I_0 \ll I_0 \quad (4.61)$$

(c) dc SQUID – dynamic case

In principle, the modulation $I_c(\Phi_a)$ can be used to measure smallest changes of the external magnetic flux.

For practical reasons, however, it is much more simple to operate the dc SQUID in the dynamic state, i.e., at $V \neq 0$ – with a constant bias current $I_B \gtrsim 2I_0$ – and to use the dependence $V(\Phi_a)$.

In the voltage state, obviously the resistances R_k and capacitances C_k of the two Josephson junctions ($k = 1, 2$) also do play a role. For the description of this situation, one uses the RCSJ model for the junctions.

The current voltage characteristics ($I - V$ curve) then modulates as a function of the external flux Φ_a between the curves shown in Fig. 4.21(b)

– with $I_{c,max} = 2I_0$ at $\Phi_a = n\Phi_0$ and $I_{c,min}$ at $\Phi_a = (n + \frac{1}{2})\Phi_0$.

At constant bias current I_B , the voltage V oscillates upon continuously changing the external flux Φ_a , along the dashed line shown in Fig. 4.21(b). This results in the $V(\Phi_a)$ characteristics as shown in Fig. 4.21(c).²⁶

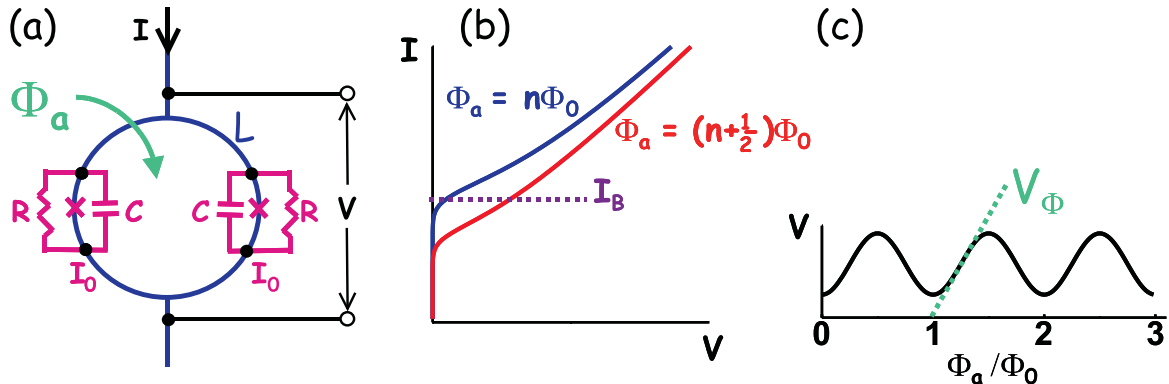


Fig. 4.21: dc SQUID: (a) schematic representation with RCSJ-junctions; (b) current-voltage characteristics; (c) voltage-flux characteristics

Hence, the voltage across the dc SQUID oscillates with the external flux with a period of Φ_0 – the dc SQUID is operated as a flux-to-voltage converter.

As a figure of merit we introduce the so-called *flux-zu-voltage transfer function* (short: transfer function). This is the slope $\partial V / \partial \Phi_a$ of the $V(\Phi_a)$ curve. Certainly, the slope depends both, on the chosen bias current, and on the working point on the Φ_a axis. Usually, one denotes the transfer function as the slope that is maximized with respect to I_B and Φ_a ²⁷, i.e.

$$V_\Phi \equiv \left(\frac{\partial V}{\partial \Phi_a} \right)_{max} . \quad (4.62)$$

²⁶In order to obtain a unique value for the voltage $V(\Phi_a)$, one uses non-hysteretic junctions, i.e. with a McCumber parameter $\beta_c \equiv \frac{2\pi}{\Phi_0} I_0 R^2 C \lesssim 1$.

²⁷Typically at $I_B \approx 2I_0$ and $\Phi_a \approx (n \pm \frac{1}{4})\Phi_0$.

A small flux change $\delta\Phi$ detected by the SQUID produces a measurable voltage change

$$\delta V = V_\Phi \cdot \delta\Phi \quad . \quad (4.63)$$

Hence, it is clear that for the optimization of the sensitivity of a SQUID, it is essential to maximize the transfer function – the latter depends in particular on the most important SQUID parameters L , I_0 and R .

A rough estimate yields for the optimum case ($\beta_L \approx 1$)

$$V_\Phi \approx \frac{\Delta V}{\frac{1}{2}\Phi_0} \approx \frac{I_0 R}{\frac{1}{2}\Phi_0} \approx \frac{R}{L} \quad . \quad (4.64)$$

\Rightarrow large R and small L , or large $I_0 R$ required !

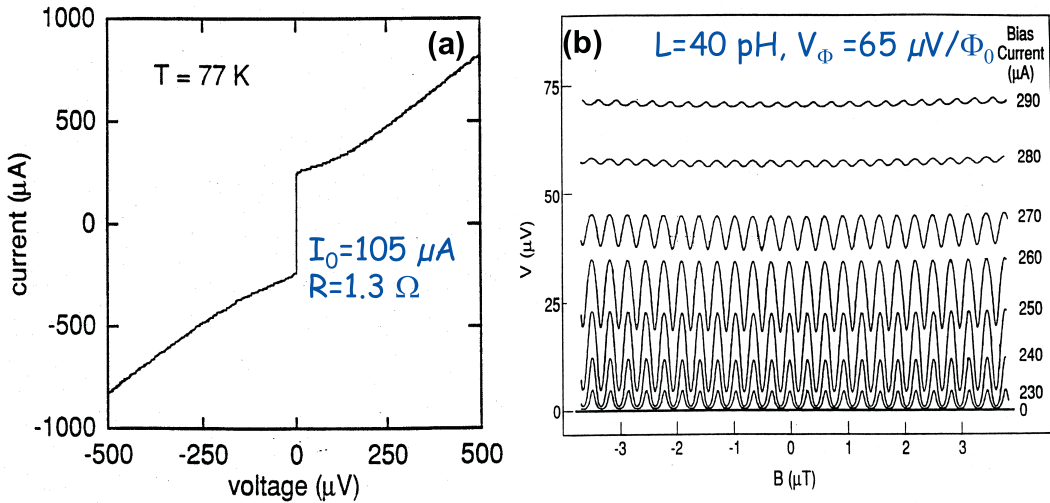


Fig. 4.22: Typical experimental result for a YBCO dc SQUID: (a) $I - V$ curve; (b) $V(\Phi)$ characteristics at different bias currents.

The intrinsic sensitivity of dc SQUIDs is determined by the thermal noise of the junction resistances at the operation temperature T . From the spectral density of voltage noise S_V of the fluctuating voltage across the SQUID, the flux noise follows as $S_\Phi = S_V/V_\Phi^2$.

The theoretical optimization of the thermal flux noise, or the energy resolution ϵ requires the (numerical) solution of the coupled equations of motion for the phase differences δ_k of the Josephson junctions. Such an analysis shows that $\beta_L \approx 1$ is optimum. For this case, one finds (in the limit of small thermal fluctuations)

$$S_\Phi \approx 16k_B T \frac{L^2}{R} \approx 8\Phi_0 k_B T \frac{L}{I_0 R} \quad \text{and} \quad \epsilon \approx 9k_B T L / R \approx \frac{9}{2} \frac{k_B T}{I_0 R} \quad . \quad (4.65)$$

C. Practical SQUIDS

(a) Fabrication and materials

Since the 1980s, dc SQUIDs are almost exclusively fabricated as thin film structures. For applications with He cooling at 4.2 K, the multilayer Nb technology with Nb/Al-AlO_x/Nb tunnel junctions (with resistive "Shunt" resistors, e.g. from PdAu) has been established.

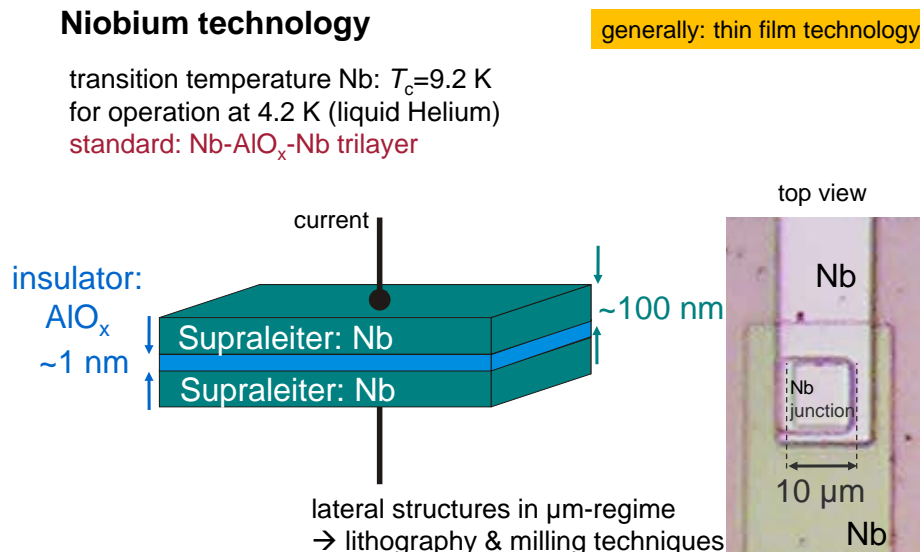


Fig. 4.23: Fabrication & materials: Nb junctions.

Cuprate-high- T_c superconductors are often developed for applications at 77 K with N₂ cooling. SQUIDs based on epitaxially grown YBCO grain boundary junctions (mostly on bicrystal substrates) yield the best results so far.

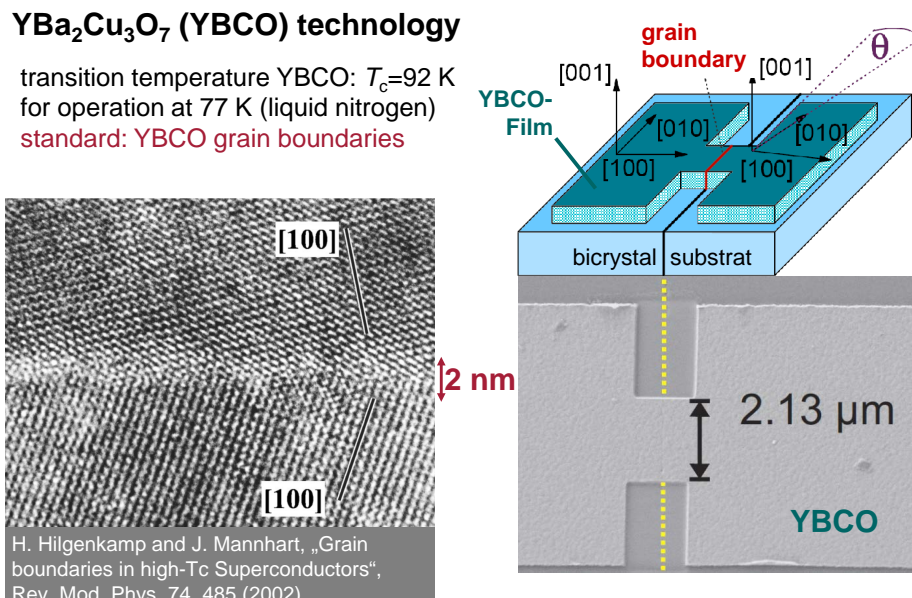


Fig. 4.24: Fabrication & materials: YBCO junctions.

Currently, intensive research is devoted to the development of strongly miniaturized SQUIDs (nanoSQUIDs) for scanning SQUID microscopy and for the investigation of smallest spin systems. Figure 4.25 shows two examples.

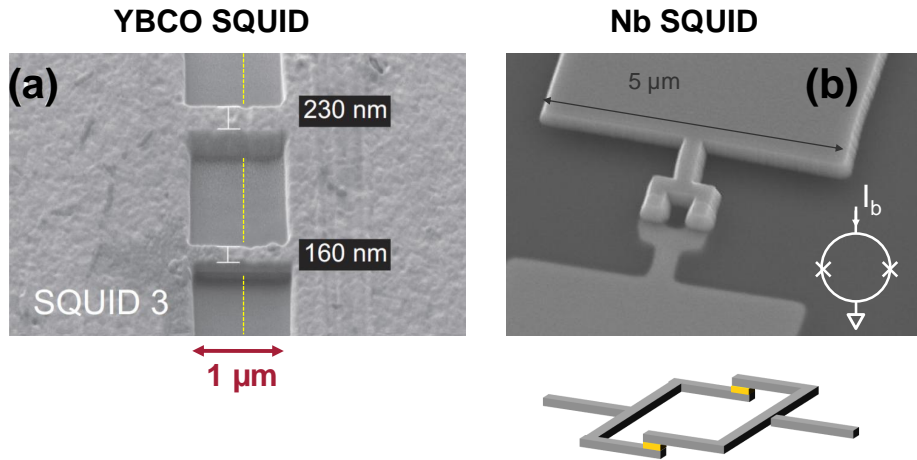


Fig. 4.25: Examples of dc SQUID structures: (a) YBCO SQUID with grain boundary junctions; the dashed line shows the position of the grain boundary in the SrTiO₃ substrate; patterning by focused ion beam (FIB) milling. (b) Nb SQUID from Nb/HfTi/Nb junctions; patterning by electron beam lithography.

(b) SQUIDs for measurements of magnetic fields and field gradients

Generally, a SQUID-based measurement system consists of three parts (see Fig. 4.26): With the help of an appropriate "input circuit", a physical quantity δx , which shall be measured, is converted into magnetic flux $\delta\Phi_a$, detected by the SQUID and converted by an appropriate readout electronics, usually into a output voltage signal δV .

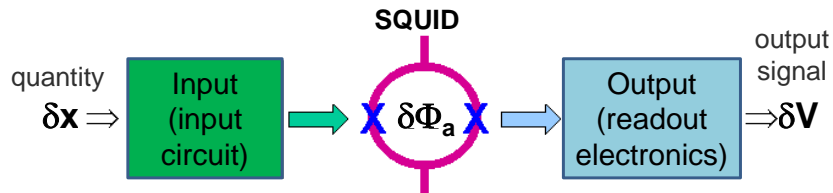


Fig. 4.26: Basic setup of a SQUID-based measurement system.

A SQUID measures with very high sensitivity the magnetic flux Φ_a through the SQUID loop. For applications, however, one is most often interested in the measurement of changes of the magnetic induction (flux density) δB . For the flux signal, which is detected by a SQUID magnetometer one has $\delta\Phi_a = \delta B \cdot A_{\text{eff}}$, with the effective magnetometer area A_{eff} . The larger the effective area, the smaller can be a change in B , which still can be detected by the SQUID (for a given sensitivity for magnetic flux). Accordingly, the sensitivity of a magnetometer is determined by the magnetic field noise $S_B^{1/2} = S_\Phi^{1/2}/A_{\text{eff}}$. Hence, the optimization of this quantity requires at the same time a small as possible SQUID inductance L (and hence a small S_Φ) and a large effective sensor area A_{eff} . This is achieved by an appropriate choice of the SQUID layout and input structures.

A typical SQUID structure, which is used for this purpose, is the so-called "washer"-SQUID.

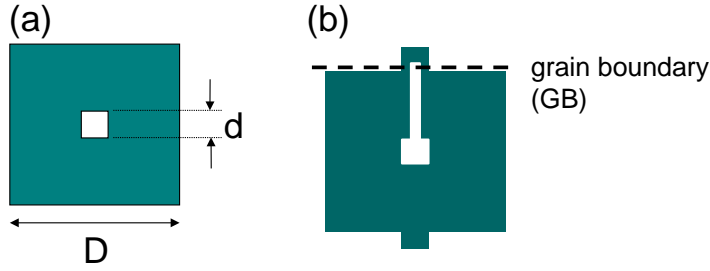


Fig. 4.27: "Washer" for flux focusing: (a) basic structure; (b) washer dc SQUID – here a version of a HTS SQUID is shown, with two Josephson junctions at the grain boundary (dashed line).

For the simple square-shaped washer structure one has:

$$L = 1.25\mu_0 d \quad \text{and} \quad A_{\text{eff}} = d \cdot D$$

Typical washer size: $d = 25 \mu\text{m}$, $D = 0.5 \text{ mm} \rightarrow A_{\text{eff}} \approx 10^{-8} \text{ m}^2$

Typical flux noise: $S_{\Phi}^{1/2} \approx 5 \mu\Phi_0/\sqrt{\text{Hz}}$

\Rightarrow magnetic field noise $S_B^{1/2} \approx 1 \text{ pT}/\sqrt{\text{Hz}}$

\rightarrow not interesting because of competing techniques, e.g. fluxgate magnetometer ('Förster-Sonde')

For the sensitive detection of magnetic fields, one uses a **superconducting flux transformer**. This consists of a pickup loop (size depends on application; typically cm diameter), which is connected in series to an input coil (typically $n = 50 - 100$ turns). A change of field δB induces a screening current I_s in the pickup loop, which also flows through the input coil and hence couples inductively the flux Φ_a into the washer SQUID.

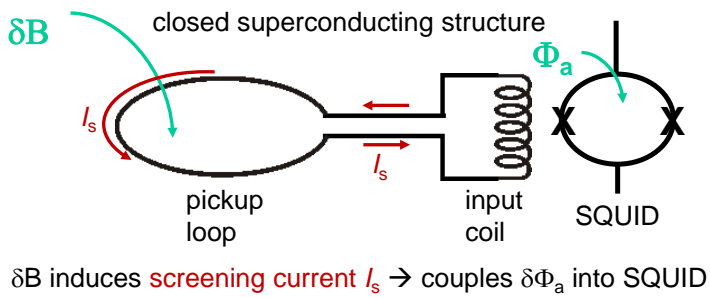


Fig. 4.28: Superconducting flux transformer with inductive coupling of the input coil to a SQUID.

For the effective area of the optimized configuration, one obtains

$$A_{\text{eff}} \approx \frac{n}{2} \alpha \frac{L}{L_p} A_p \quad , \quad (4.66)$$

with number of turns n of the input coil, coupling factor $\alpha \leq 1$, and A_p , L_p are the area and inductance of the pickup loop, respectively. With typical values $n = 50$, $\alpha = 0.7$, $L = 100 \text{ pH}$, $L_p = 10 \text{ nH}$, $A_p = 1 \text{ cm}^2$ follows $A_{\text{eff}} \approx 10^{-5} \text{ m}^2$
 \rightarrow factor ~ 1000 as compared to washer SQUID.

In order to obtain an as large as possible coupling factor α , the input coil is directly deposited by thin film technology on top of the thin film washer SQUID (separated by an insulating interlayer) → "Ketchen magnetometer".

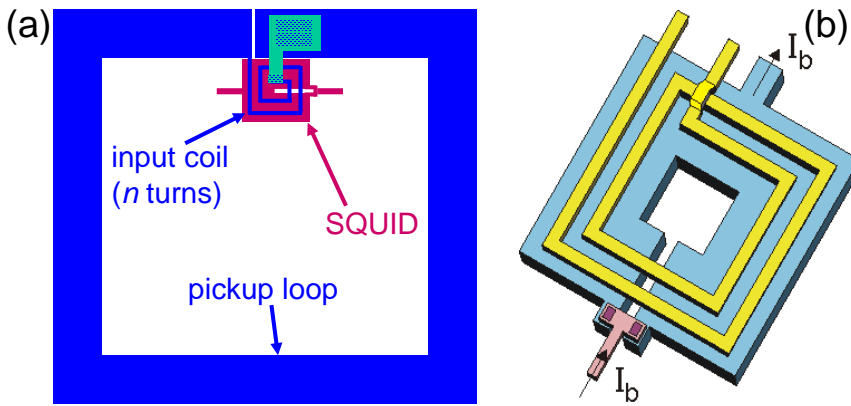


Fig. 4.29: Inductively coupled magnetometer (Ketchen magnetometer): (a) complete structure consisting of flux transformer and washer SQUID; (b) input coil of the flux transformer above the washer SQUID.

With such an arrangement, produced in Nb technology, routinely SQUID magnetometers with a sensitivity of $S_B^{1/2} \approx 1 \text{ fT}/\sqrt{\text{Hz}}$ at $T = 4.2 \text{ K}$ are realized. For comparison: 1fT is by a factor of 6×10^{10} smaller than the earth's magnetic field. An alternative concept relies on the parallel arrangement of m loops in a SQUID ("multiloop SQUID", "cart wheel SQUID"). Also this arrangement allows for the realization of magnetometers with a field sensitivity comparable to that of the Ketchen magnetometer.

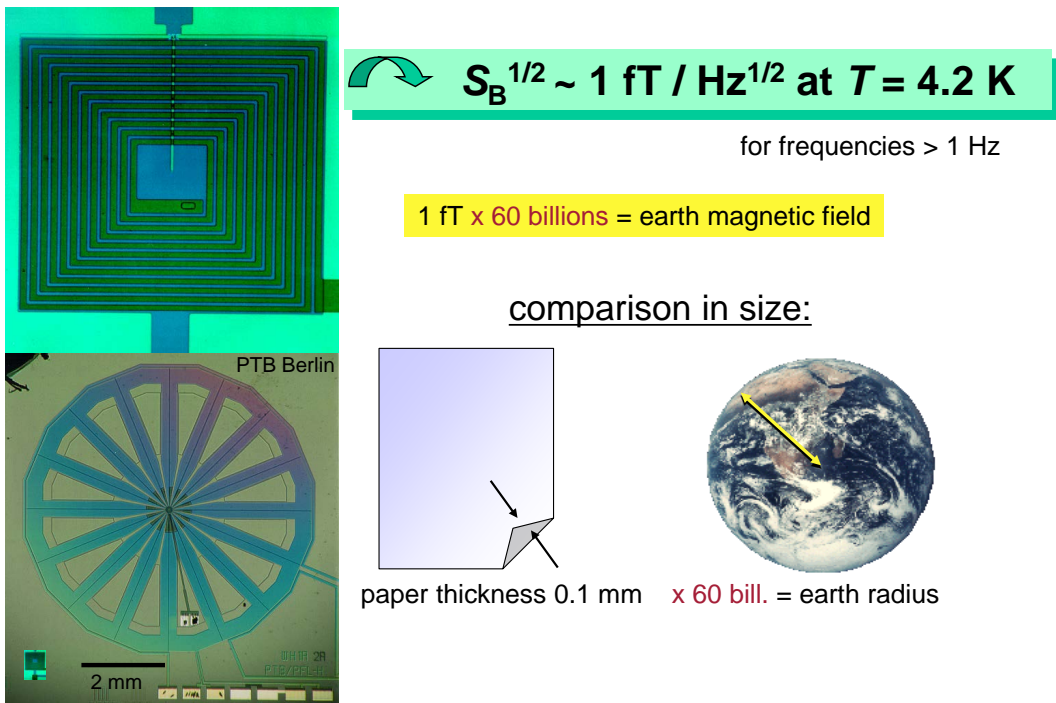
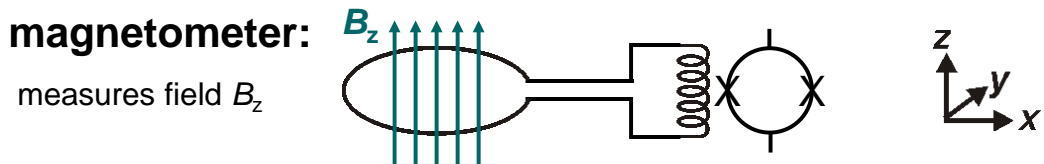


Fig. 4.30: SQUID magnetometer in Ketchen design (upper left) or as multiloop SQUID (lower left) reach extremely high field sensitivity at 4.2 T.

A gradiometric arrangement of the pick-up loops enables the measurement of magnetic field gradients.

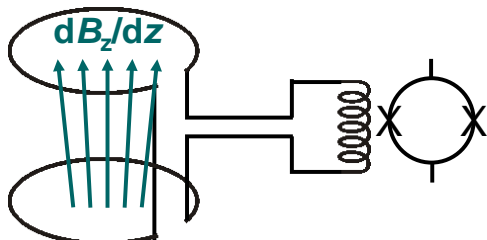
→ detector is insensitive to spatially homogeneous disturbing fields!

In Nb technology, wire-wound pickup loops can be used, which have a superconducting connection to the Nb chips with input coil and SQUID washer.



1. order gradiometer:

counter-wound
pickup-loops:



measures gradient dB/dz
→ local signals at one loop

**insensitive against
homogeneous
disturbing fields !!**

Fig. 4.31: SQUID gradiometer: While a magnetometer with a simple pickup loop in the x, y -plane detects the field component B_z , a serial arrangement of two oppositely wound pickup loops allows for the detection of the gradient $\partial B_z / \partial z$. The gradiometric arrangement is insensitive against homogeneous disturbing fields and, hence, only sensitive for local fields in close vicinity to one of the two pickup loops.

D. SQUID applications

Overview

Ultra-sensitive measurements of a variety of physical quantities, which can be converted into magnetic flux.

- | | quantities |
|---|---|
| • Biomagnetism | $\rightarrow I, B, \nabla B$
$\rightarrow M$ |
| → <i>non-invasive imaging of brain and heart activity,</i> | |
| → <i>magnetic resonance imaging (MRI) at low magnetic fields</i> | |
| • Geophysics | $\rightarrow B, \nabla B$ |
| → <i>search for fossile or geothermal energy resources, ...</i> | |
| • Non-destructive evaluation of materials | $\rightarrow I, B, \nabla B$ |
| → <i>cracks or magnetic inclusions (airplane wheels, -turbines, reinforced steel in bridges), ...</i> | |
| • Magnetometry, Susceptometry | $\rightarrow M, \chi$ |
| → <i>materials-/geosciences</i> | |
| → <i>magnetic nanoparticles/molecules</i> → nanoSQUIDs | |
| • Metrology | $\rightarrow V_{dc}, V_{rf}, I, T$ |
| → <i>voltmeter, amperemeter, noise thermometer, ...</i> | |
| • Gravitational wave & particle detectors | $\rightarrow \delta\ell, \delta T$ |
| • SQUID microscopy | $\rightarrow B, \Phi(x,y,z)$ |

The area of biomagnetism comprises the detection of magnetic fields (currents, magnetic particles, nuclear spins) in living organisms, in particular in humans.

- Magneto-encephalography (MEG) → brain currents
- Magneto-cardiography (MCG) → heart currents
- Magneto-neurography (MNG) → action currents in nerves
- Liver-susceptometry → the only non-invasive method for quantitative determination of Fe-concentration in the liver
- Magneto-gastrography (MGG) & -enterography (MENG)
 - currents due to spontaneous activity of stomach & intestine muscles (MGG)
 - magnetic marker → mobility/transport in stomach-intestine (MENG)
- Magnetic relaxation immunoassays (MARIA)
 - magnetic relaxation of marker, coupled to antibodies
 - detection of smallest concentrations of specific substances (hormone, virus, ...)
- Low-field magnetic resonance imaging (MRI)
 - simpler MRI systems; cancer diagnosis

Biomagnetism belongs to the most important fields of applications for SQUIDs. This includes in particular the detection of extremely small magnetic fields generated by brain currents, which cannot be detected by conventional methods.

Problem:

Signals are superimposed on enormously strong disturbing fields (for examples see Fig. 4.32) – requires magnetic shielding and/or compensation techniques (hardware and software).

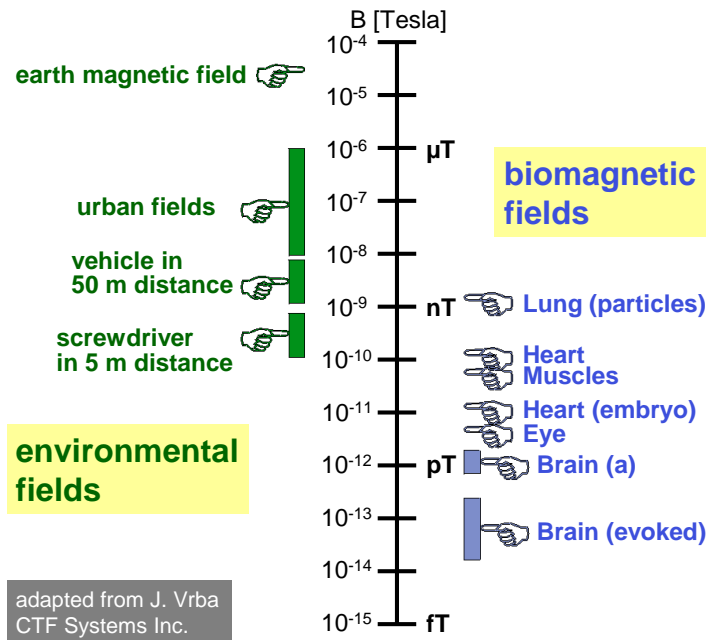


Fig. 4.32: magnetic fields for SQUID applications in biomagnetism.

Magneto-encephalography (MEG)

MEG poses the highest requirements on the sensitivity of SQUID magnetometers; typical signal levels to be detected are in the pT to fT range.

A key advantage, as compared to the electric detection of potentials on the head by electro-encephalography (EEG), lies in the fact that the detected magnetic fields are not distorted by tissue and the skull.

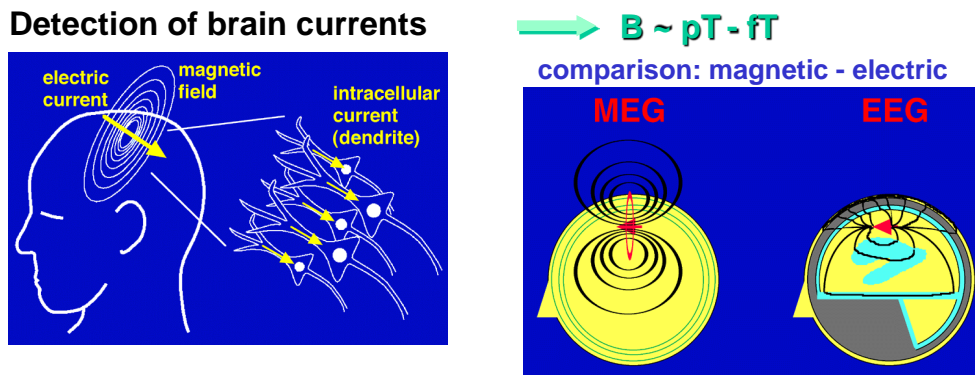


Fig. 4.33: Comparison MEG with EEG [from CTF Systems Inc: MEG Introduction: Theoretical Background (2001); <http://www.ctf.com>].

Further advantages of MEG lie in the possibility, by using multi-channel systems (>100 sensors), to exploit MEG as a contactless, non-invasive imaging method. In comparison to EEG imaging, this method is significantly faster.

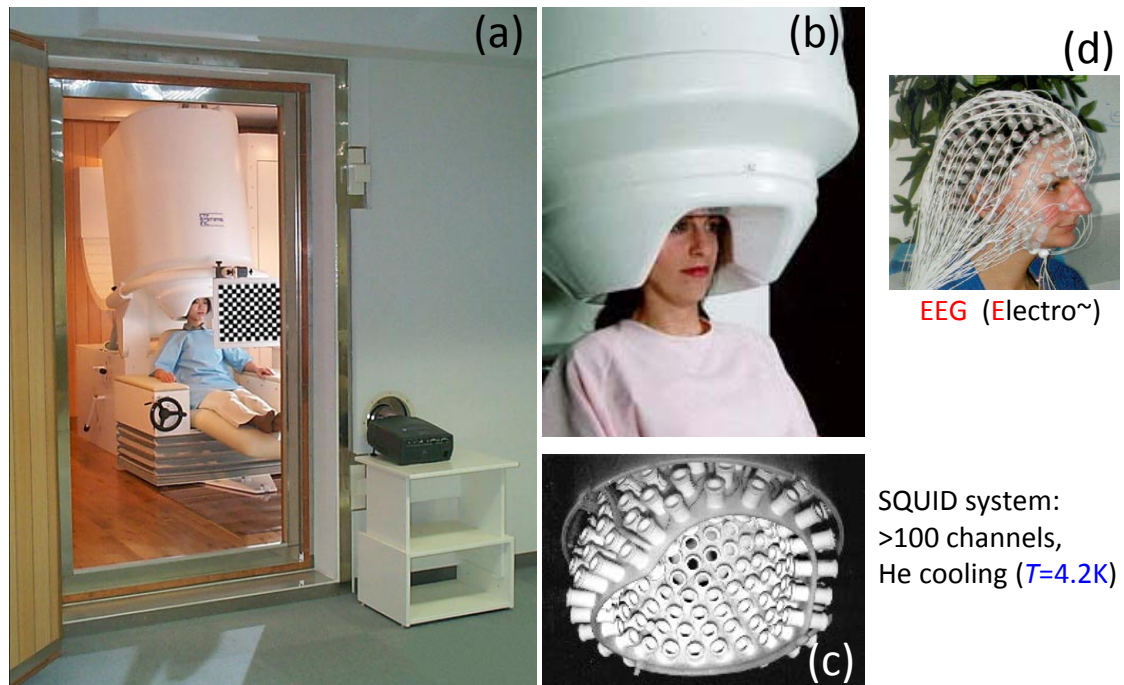


Fig. 4.34: MEG system: (a) in magnetically shielded room, (b) section shows helmet system with dewar; (c) cross-section through the helmet-like sensor arrangement; (d) for comparison: EEG arrangement [from Buckel, Kleiner, Wiley-VCH (2004)].

MEG is used, e.g., for the diagnosis of focal epilepsy (see Fig. 4.35), or for presurgical mapping of brain tumors.

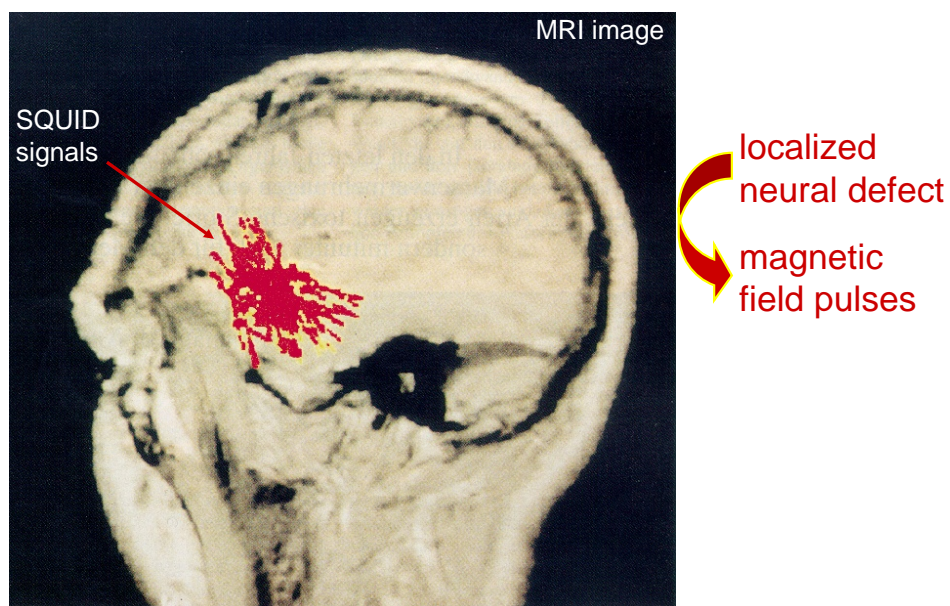


Fig. 4.35: Magneto-encephalography (MEG) for the diagnosis of focal epilepsy [from J. Clarke, Scientific American 08/1994].

Magnetic resonance imaging (MRI) in low fields

A very recent development concerns the use of SQUIDs (instead of normal conducting induction coils) as sensors for magnetic resonance imaging (MRI).

In comparison to conventional MRI in very strong magnetic fields of several Tesla, the use of SQUIDs allows for the operation in fields which are by approximately for orders of magnitude lower → μ Tesla-MRI.

conventional Tesla-MRI:

detection of magnetization of proton spins in magnetic field B_0
at frequencies $f = B_0 \cdot 42.6$ MHz/T with induction coils

→ signal $U_{\text{ind}} \sim f B_0 \sim B_0^2$

→ enormously high requirements for homogeneity of B_0



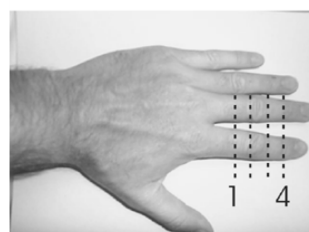
low-field (μ Tesla)-MRI:

detection at kHz-frequencies with SQUIDS → signal $\delta\Phi$ independent of f

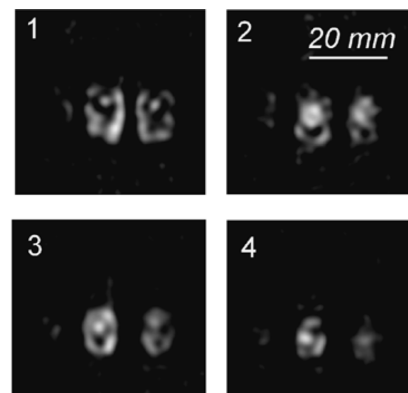
→ enormous potential for „simple“ MRI systems



M. Mössle, UC Berkeley



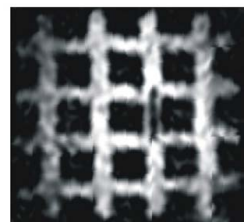
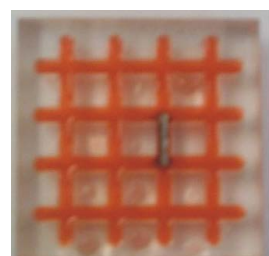
$B_0 = 132 \mu\text{T}$



further advantages:

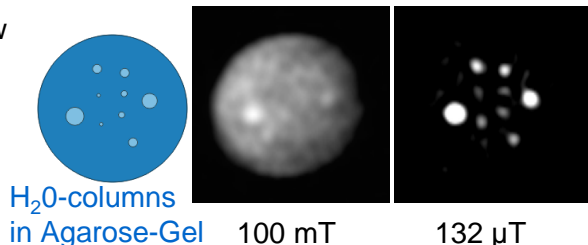
avoids artefacts from metallic objects

→ monitoring of biopsies



enhanced image contrast at low fields/frequencies

→ cancer diagnosis

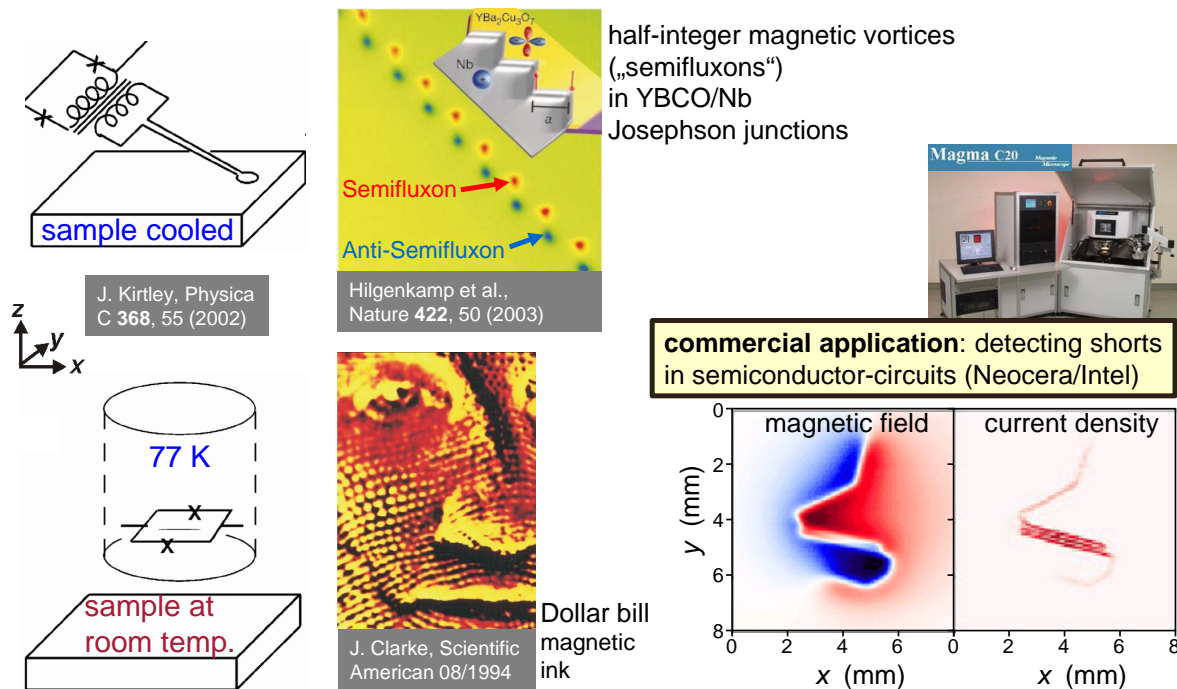


M. Mössle, UC Berkeley

Scanning SQUID microscopy

Scanning SQUID microscopy combines the high flux sensitivity of SQUIDs with a steadily improving spatial resolution (typical resolution $1\text{ }\mu\text{m}$).

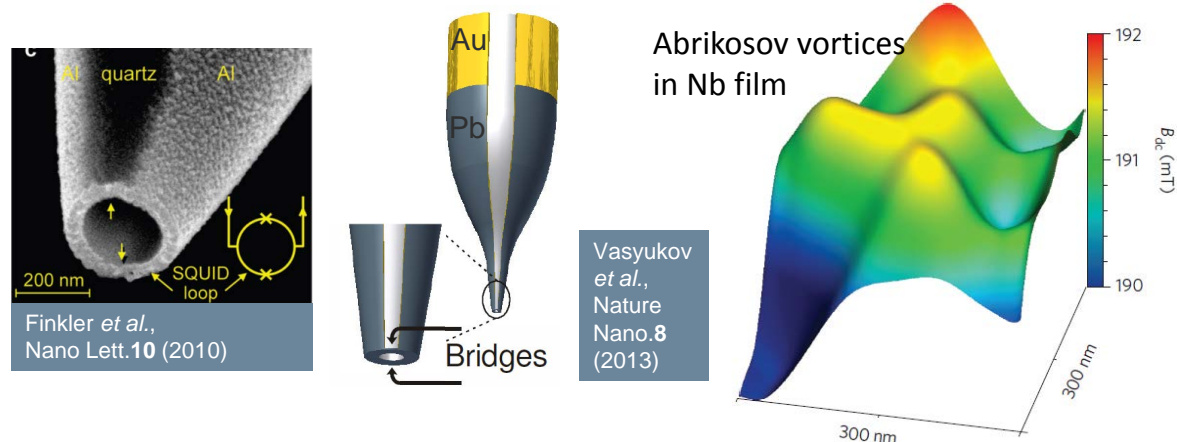
Here, a SQUID, or the pickup loop of a flux transformer that is inductively coupled to a SQUID, is scanned in as small as possible distance above the sample to be investigated.



With the development of the SQUID-on-tip (SOT), extremely small SQUIDs (down to 50 nm diameter) became available as sensors for SQUID microscopy in 2013. With such a SOT, a drastically improved spatial resolution of approximately 100 nm has been demonstrated, for the imaging of superconducting structures at 4.2 K.

SQUID-on-tip (SOT)

shadow evaporation of superconducting film (Al, Pb, Nb) onto apex of nanotip
 \rightarrow SQUID loop with constriction junctions (no lithography required!)



Mirco- and nanoSQUIDs for investigations of magnetic nanoparticles

For the detection of tiny magnetic moments of *individual* magnetic nanoparticles (MNPs), strongly miniaturized microSQUIDs have been developed by W. Wernsdorfer *et al.*²⁸

For this application of SQUIDs, a MNP has to be placed as close as possible to the SQUID loop. By applying an external magnetic field H in the loop plane, the magnetic moment μ can be switched, which induces a change of stray magnetic field from the MNP coupled to the SQUID (see Fig. 4.36). This way, the magnetization M vs H loop of the MNP can be traced out, which allows investigations of magnetization reversal processes in single MNPs.

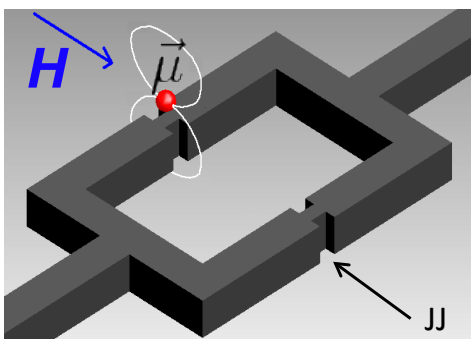


Fig. 4.36: Principle of detection of the magnetic moment μ of a MNP placed on top of a SQUID.

The figure of merit, regarding sensitivity of this kind of SQUID application, is the spin sensitivity $S_\mu^{1/2} = S_\Phi^{1/2}/\phi_\mu$. This quantity is determined by the spectral density of flux noise S_Φ of the SQUID and by the coupling factor $\phi_\mu = \Phi/\mu$. The coupling factor quantifies the change of magnetic flux Φ coupled to the SQUID by the MNP per magnetic moment μ of the MNP.

With the scaling $S_\phi \propto k_B T L / (I_0 R)$ from Eq. (4.65), it is clear that the flux noise of the SQUID can be improved by reducing its inductance L , i.e. by shrinking the size of the SQUID loop. As a consequence, during the last decade even smaller SQUIDS – so-called *nanoSQUIDs* – have been developed, with steadily improving flux noise and spin sensitivity.²⁹ So far, the lowest value $S_\mu^{1/2} \sim 0.4 \mu_B/\text{Hz}^{1/2}$ (μ_B is the Bohr magneton) at $T = 4 \text{ K}$ has been obtained with a Pb-SOT with $\sim 50 \text{ nm}$ loop diameter (calculated for a MNP placed in the center of the loop).

Measurements of $M(H)$ loops on single MNPs with micro- or nanoSQUIDs enable investigations on the magnetic anisotropy of such particles (details on the magnetic anisotropy of MNPs will be treated in chapter 6). Ideally, one would like to detect simultaneously all three components of the vector magnetic moment $\mu = (\mu_x, \mu_y, \mu_z)$ upon magnetization reversal of a MNP. This can be achieved with the 3D vector nanoSQUID which has been realized very recently.³⁰ Such a device contains three nanoSQUIDs

²⁸W. Wernsdorfer, *Classical and quantum magnetization reversal studied in nanometersized particles and clusters.*, Adv. Chem. Phys. **118**, 99–190 (2001); W. Wernsdorfer, *From micro- to nano-SQUIDs: applications to nanomagnetism*, Supercond. Sci. Technol. **22**, 064013 (2009).

²⁹C. Granata and A. Vettoliere, *Nano superconducting quantum interference device: A powerful tool for nanoscale investigations*, Phys. Rep. **614**, 1–69 (2016); M. J. Martínez-Pérez, R. Kleiner, D. Koelle, *NanoSQUIDs Applied to the Investigation of Small Magnetic Systems*, chapter 19 in A. V. Narlikar, (editor), *The Oxford Handbook of Small Superconductors*, Oxford University Press (2017).

³⁰M. J. Martínez-Pérez *et al.*, Three-Axis Vector Nano Superconducting Quantum Interference Device, ACS Nano **10**, 8128–8123 (2016).

(SQ_x , SQ_y , SQ_z) with orthogonal SQUID loops that can detect the magnetic moments μ_x , μ_y , μ_z of a MNP placed in the center of the (gradiometric) nanoSQUID SQ_z . This design can be used for switching the magnetic moment of the MNP in a magnetic field \mathbf{H} applied in z direction. The 3D vector nanoSQUID shown in Fig. 4.37 is based on Nb nanoSQUIDs with SNS Josephson junctions based on Nb/HfTi/Nb trilayers.

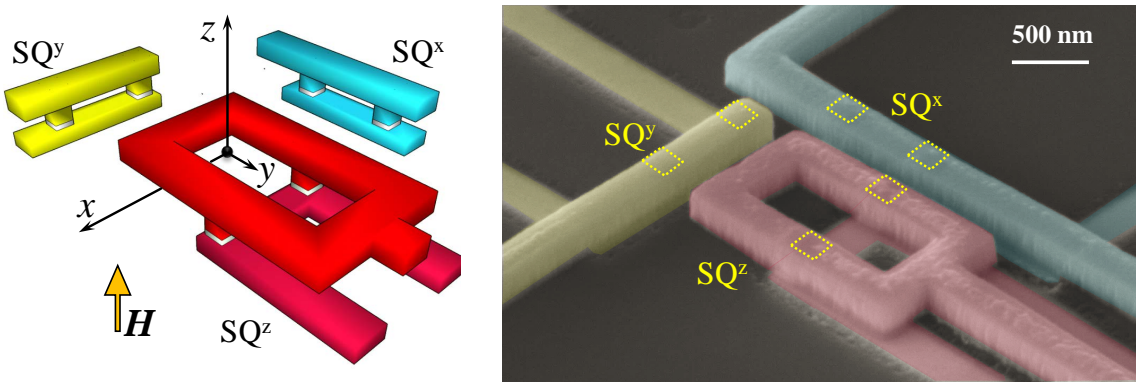


Fig. 4.37: Vector nanoSQUID: Schematic layout (left) and SEM image (right).

Measurements on MNPs with micro- or nanoSQUIDs based on conventional metallic superconductors (e.g. Nb) are restricted to temperatures of a few K and below. Moreover, the maximum magnetic fields such SQUIDs can sustain are limited by the upper critical field B_{c2} of those materials to $\lesssim 1$ T. Therefore, the use of YBCO – with much higher $T_c \sim 90$ K and $B_{c2} \gtrsim 40$ T is quite promising for the realization of nanoSQUIDs. YBCO nanoSQUIDs with grain boundary Josephson junctions have been realized by nanopatterning with a Ga focused ion beam (FIB). Spin sensitivities down to $\sim 4 \mu_B/\text{Hz}^{1/2}$ at 4.2 K³¹ and operation in strong fields up to 3 T has been demonstrated.³² Very recently, such YBCO nanoSQUIDs have been used to investigate the thermally activated magnetization reversal processes of Co MNPs which have been grown directly on top of the nanoSQUIDs.³³

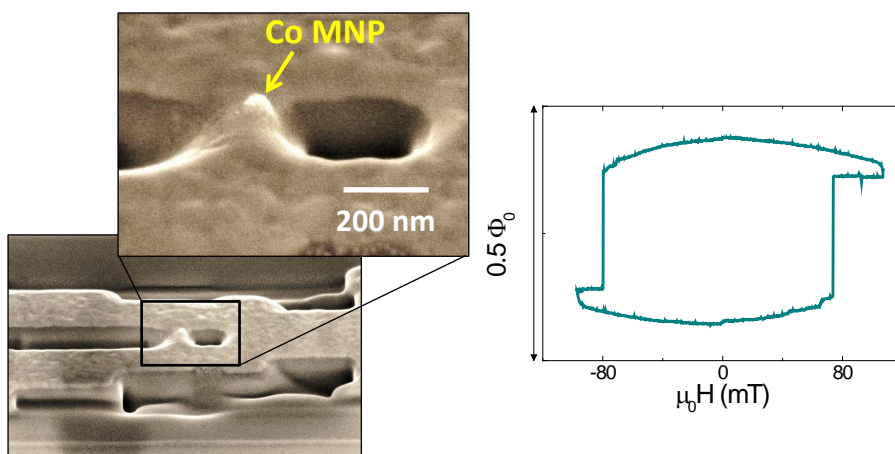


Fig. 4.38:
Left: YBCO nanoSQUID with Co MNP; right: $\Phi(H)$ hysteresis loop of Co MNP.

³¹T. Schwarz *et al.*, Low-Noise $YBa_2Cu_3O_7$ NanoSQUIDs for Performing Magnetization-Reversal Measurements on Magnetic Nanoparticles, *Phys. Rev. Appl.* **3**, 044011 (2015).

³²T. Schwarz *et al.*, Low-Noise Nano Superconducting Quantum Interference Device Operating in Tesla Magnetic Fields, *ACS Nano* **7**, 844–850 (2015).

³³M. J. Martínez-Pérez *et al.*, NanoSQUID magnetometry of individual cobalt nanoparticles grown by focused electron beam induced deposition, *Supercond. Sci. Technol.* **30**, 024003 (2017).

